SANDIA REPORT

SAND2007-5941
Unlimited Release
Printed September, 2007

Atomically Engineering Cu/Ta Interfaces

X. W. Zhou, E. B. Webb III

Prepared by
Sandia National Laboratories
Albuquerque, New Mexico 87185 and Livermore, California 94550

Sandia is a multiprogram laboratory operated by Sandia Corporation,
a Lockheed Martin Company, for the United States Department of Energy's
National Nuclear Security Administration under Contract DE-AC04-94-AL85000.

Sandia National Laboratories

Issued by Sandia National Laboratories, operated for the United States Department of Energy by Sandia Corporation.

Available to DOE and DOE contractors from
U.S. Department of Energy
Office of Scientific and Technical Information
P.O. Box 62
Oak Ridge, TN 37831

Telephone: (865) 576-8401
Facsimile: (865) 576-5728
E-Mail: reports@adonis.osti.gov
Online ordering: http://www.osti.gov/bridge

Available to the public from
U.S. Department of Commerce
National Technical Information Service
5285 Port Royal Rd
Springfield, VA 22161

Telephone: (800) 553-6847
Facsimile: (703) 605-6900
E-Mail: orders@ntis.fedworld.gov
Online ordering: http://www.ntis.gov/help/ordermethods.asp?loc=7-4-0#online

SAND2007-5941
Unlimited Release
Printed September, 2007

Atomically Engineering Cu/Ta Interfaces

Xiao Wang Zhou
Mechanics of Materials Department
Sandia National Laboratories
P.O. Box 969 - MS 9402
Livermore, California 94550
xzhou@sandia.gov

Edmund B. Webb III
Computational Materials Science and Engineering Department
Sandia National Laboratories
P. O. Box 5800 - MS 1411
Albuquerque, NM 87123
ebwebb@sandia.gov

Abstract

This report summarizes the major research and development accomplishments for the late start LDRD project (investment area: Enable Predictive Simulation) entitled "Atomically Engineering Cu/Ta Interfaces". Two ultimate goals of the project are: (a) use atomistic simulation to explore important atomistic assembly mechanisms during growth of Cu/Ta multilayers; and (b) develop a non-continuum model that has sufficient fidelity and computational efficiency for use as a design tool. Chapters 2 and 3 are essentially two papers that address respectively these two goals.

In chapter 2, molecular dynamics simulations were used to study the growth of Cu films on (010) bcc Ta and Cu_xTa_{1-x} alloy films on (111) fcc Cu. The results indicated that fcc crystalline Cu films with a (111) texture are always formed when Cu is grown on Ta. The Cu films are always polycrystalline even when the Ta substrate is single crystalline. These polycrystalline films are composed of grains with only two different orientations, which are separated by either orientational grain boundaries or misfit dislocations. Periodic misfit dislocations and stacking fault bands are observed. The Cu film surface roughness was found to decrease with increasing adatom energy. Due to a Cu surface segregation effect, the Cu_xTa_{1-x} films deposited on Cu always have a higher Cu composition than that used in the vapor mixture. When Cu and Ta compositions in the films are comparable, amorphous structures may form. The fundamental origins for all these phenomena have been studied in terms of crystallography and interatomic interactions.

In chapter 3, a simplified computational method, diffusional Monte Carlo (dMC) method, was developed to address long time kinetic processes of materials. Long time kinetic processes usually involve material transport by diffusion. The corresponding microstructural evolution of materials can be analyzed by kinetic Monte Carlo simulation methods, which essentially simulate structural evolution by tracing each atomic jump. However, if the simulation is carried out at a high temperature, or a jump mechanism with a very low energy barrier is encountered, the jump frequency may approach the atom vibration frequency, and the computational efficiency of the kinetic Monte Carlo method rapidly decreases to that of a molecular dynamics simulation. The diffusional Monte Carlo method addresses the net effects of many atom jumps over a finite duration, kinetically controlled process. First, atom migration due to both random and non-random jumps is discussed. The concept of dMC is then introduced for random jump diffusion. The validity of the method is demonstrated using several diffusion cases in one-, two- and three- dimensional spaces, including the dissolution of spinodal structures. The application of the non-random diffusion theory to spinodal decomposition is also demonstrated.

Keywords: Ta/Cu multilayer, MD simulation, surface roughness, grain structure, misfit dislocation, stacking fault, amorphization, diffusional Monte Carlo method

Acknowledgment

Contributions from J. J. Quan, M. Francis, H. N. H. Wadley, and M. N. Neurock at University of Virginia are greatly acknowledged.

This page intentionally left blank.

Contents

List of Figures

Chapter 1

Introduction

Atomic scale interfaces are essential to nanotechnologies that exploit high interfacial area to system volume ratios. For instance, creation of a bimodal distribution of grain boundaries in nanocrystalline metals (e.g., copper, aluminum, etc.) significantly improve both strength and ductility of the materials.[1] Control of interfacial structures is essential for multilayered thin film solar cells.[2] Other vapor deposited multilayer structures, such as giant magnetoresistance multilayers,[3, 4, 5] magnetic tunnel junction multilayers,[6, 7, 8] X-ray mirror multilayers,[9] and microelectronic multilayers,[10, 11], all require chemically sharp, uniform interfaces. The atomic scale structures of the interfaces formed during vapor deposition process, are determined by complicated thermodynamic and kinetic processes that are extremely sensitive to interrelated processing conditions, material properties, surface chemistry, and crystal orientations. Because the fundamental origins for the formation of atomic interfacial structures are complicated and are not well understood, the current application of many nanotechnologies is far below their potentials. Understanding atomic assembly mechanisms via the study of a few representative interfacial systems could be vital to many of the nanotechnologies.

Copper/tantalum (Cu/Ta) multilayer system is a good example for study. This system is of particular interest for two important reasons. First, Ta is an effective barrier to Cu diffusion. The insertion of a thin Ta layer between Cu and semiconductors would then enable Cu to be used as interconnects in large scale integrated circuits without Cu diffusion into the semiconductor devices.[12] The low electrical resistance of Cu promises a significant improvement in device performance over more conventional Al interconnects. Second, amorphous films can be obtained during growth of Cu/Ta multilayers.[13, 14, 15] Amorphous metals have high strength, high corrosion resistance, and special magnetic properties suited for communication, aerospace, military, and transport applications.[16, 17, 18] Cu interconnects require sharp crystalline Cu/Ta interfaces, while amorphization requires highly mixed interfaces. Both types of interfaces can be synthesized through physical vapor deposition. Vastly different interfaces arise from many interrelated factors including interfacial roughness/mixing, point/extended defects, relative Cu and Ta crystallographic orientations, growth sequence (Cu on Ta or Ta on Cu), film composition, and growth conditions (e.g., adatom energy, adatom incident angle, substrate temperature, growth rate, and inert gas ion assistance etc.). Because this system enables the fundamental origins for a wide spec-

trum of atomic scale interfaces to be explored, it may provide the essential knowledge for many nanotechnologies.

Molecular dynamics (MD) simulation is a highly desired approach to study the growth of multilayers as it can accurately predict the atomic assembly mechanisms and the origins of the formation of different atomic scale interfaces provided that a high fidelity interatomic potential is used. MD, however, cannot address long time kinetics problems due to a very high computational cost. The use of MD in the simulation of thin film growth is therefore limited to accelerated growth rates that can be up to ten orders of magnitude higher than those used in experiments. Long time scale simulation methods are needed to compliment an MD analysis. Here we carry out MD simulations to explore surface roughness, grain structure, misfit dislocation, and amorphization as well as their formation mechanisms during growth of Cu films on Ta and Cu-Ta alloy films on Cu. We also attempt to develop a simplified computational method for studying long time kinetics problems.

Chapter 2

Atomic Assembly of Cu/Ta Multilayers: Surface Roughness, Grain Structure, Misfit Dislocation, and Amorphization

Gong and Liu have used a Finnis-Sinclair potential in molecular dynamics (MD) simulations to explore relative stabilities of various combinations of manually created interfaces between Cu and Ta (100), (110), and (111) atomic planes.[19, 20] They found that the energy of unstable interfaces can be sufficiently large to drive interdiffusion of Cu and Ta and cause solid state amorphization. However, it is not clear how an unstable interface can form during deposition in the first place. Molecular dynamics simulations of growth of Cu/Ta multilayers have also been carried out by a continuous injection of adatoms to the growth surface.[21] The approach created more realistic interfaces and shed light on atomic assembly mechanisms during growth and the formation of solid-state amorphization. However, the effect of vapor phase composition was not explored and the computational size was too small to reveal realistic atomic assembly phenomena. The present work carries out larger scale molecular dynamics simulations of Cu/Ta multilayer growth to study the formation of different Cu/Ta interface morphologies and grain structures as a function of conditions and vapor phase composition. These phenomena were unlikely to be accurately revealed in previous, smaller scale simulations[21]. Through collaboration with the University of Virginia, selected experiments were also carried out to verify the results of our simulations.

2.1 Embedded Atom Method Potential

The interatomic interactions between metal atoms can be well described by the embedded atom method (EAM) potentials.[22] A literature embedded atom method interatomic potential database has included 16 metal elements (Cu, Ag, Au, Ni, Pd, Pt, Al, Pb, Fe, Mo, Ta, W, Mg, Co, Ti, and Zr) and their alloys.[23, 24] This potential database has been successfully applied to simulate the growth of a number

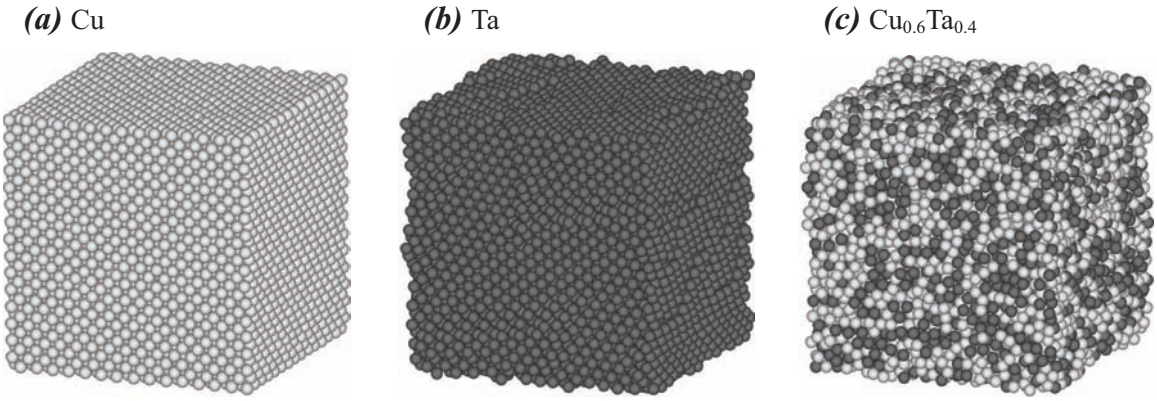

Figure 2.1. Atomic images of (a) Cu; (b) Ta; and (c) $Cu_{0.6}Ta_{0.4}$ bulk structures after the two-step energy minimization simulations.

of metal multilayers.[23, 25] The same potential was hence used in this study. The potential was well fitted to the lattice constant, cohesive energy, elastic constants, and vacancy formation energy of elements.[23, 24] The cross pair potentials between dissimilar species were not fitted. Instead, they were constructed based upon an alloy embedded atom method model.[26], and were found to realistically predict the heat of mixing of many selected binary systems. To characterize the behavior of the potential for the present case, we calculate the heat of mixing of Cu-Ta alloy.

A series of fcc substitutional Cu_xTa_{1-x} ($0 \leq x \leq 1$) crystals were used as initial configurations to evaluate the heat of mixing. The cubic computational cell was assumed to be in the cubic crystal orientation (i.e., x - [100], y - [010], z - [001]). The lattice contains a total of 13500 atoms. The systems were treated as infinitely large bulk by using periodic boundary conditions in all three coordinate directions. To ensure a full relaxation of the systems, two-step simulations were used: First, a simulated-annealing was carried out for a nanosecond of simulated (real) time using zero pressure molecular dynamics simulations where the system was slowly cooled down to 300 K from an initial temperature of 800 K. Second, zero pressure molecular statics was carried out to further minimize the potential energy of the system. Figs. 2.1(a), 2.1(b), and 2.1(c) show respectively the images of Cu, Ta and $Cu_{0.6}Ta_{0.4}$ structures after the energy minimization simulations. Not all systems maintained their original crystal configurations. It can be seen that while Cu remained a perfect fcc phase, Fig. 2.1(a), the initial fcc Ta transformed to multiple domains separated by boundaries, Fig. 2.1(b). Analysis showed that these domains are bcc crystalline grains. This is expected as bcc Ta has a lower cohesive energy than fcc Ta. Finally, the $Cu_{0.6}Ta_{0.4}$ system was found to transform to an amorphous structure, Fig. 2.1(c). To confirm these observations, radial distribution functions were calculated for systems with different compositions, and selected results are shown in Fig. 2.2. The peak neighbor distances shown in Fig. 2.2 clearly indicate that the Cu remained an fcc

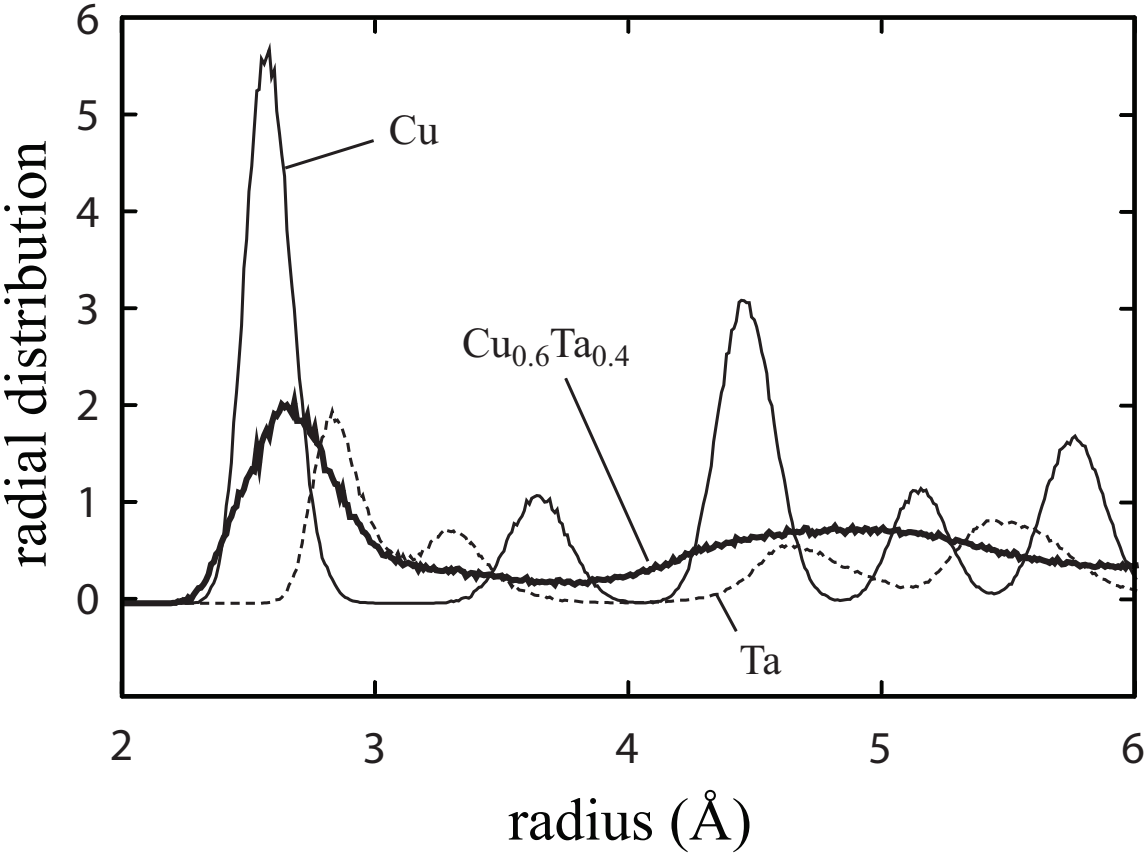

Figure 2.2. Radial distribution functions for selected bulk phases.

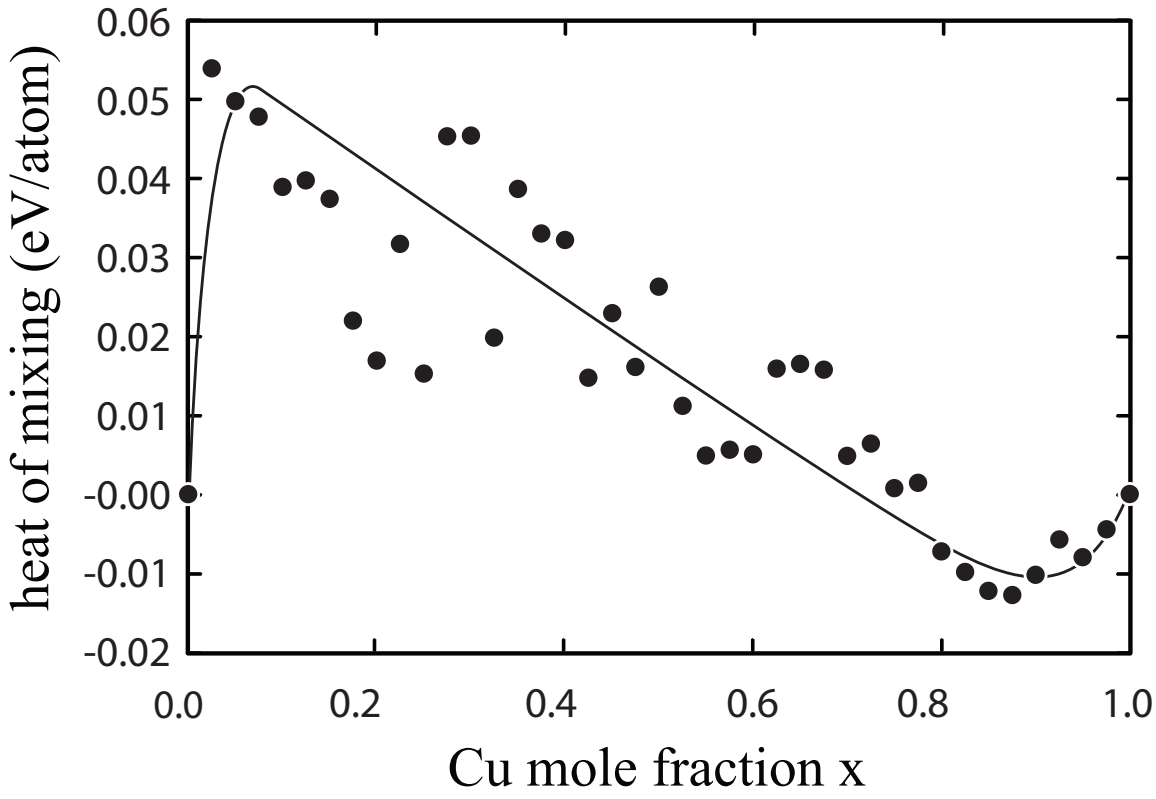

Figure 2.3. Heat of mixing as a function of composition.

crystal, and Ta transformed to a bcc structure. There is no peak distribution for the next nearest neighbor distance for the $Cu_{0.6}Ta_{0.4}$ structure, indicating that it lost its long-range ordering and became amorphous.

The procedure used above only identified a local minimum of the Ta energy because the elimination of domain (grain) boundaries requires energy activation. As a result, we created a body-centered-cubic (bcc) Ta to calculate the energy for Ta. The computational cell of the bcc Ta has a cubic dimension, a cubic crystal orientation, and 2000 atoms. The heat of mixing ΔH_{mix} was calculated as

$$\Delta H_{mix} = E_{Cu_xTa_{1-x}} - x \cdot E_{fcc\ Cu} - (1-x) \cdot E_{bcc\ Ta} \tag{2.1}$$

where $E_{Cu_xTa_{1-x}}$, $E_{fcc\ Cu}$, and $E_{bcc\ Ta}$ are the minimized potential energy per atom (i.e., cohesive energy) of Cu_xTa_{1-x}, fcc Cu, and bcc Ta phases respectively. The results of heat of mixing as a function of Cu mole fraction x is shown in Fig. 2.3. Fig. 2.3 indicates that the potential correctly captures a positive heat of mixing when the Cu composition in the alloy is low.[14, 19] The heat of mixing at x = 0.5 is between 0.01 and 0.02 eV/atom. This is a little smaller than the 0.03 eV/atom predicted by another EAM potential.[21] Our result is likely to be well relaxed as the two-step simulations enabled phase transformation whereas the previous work constrained the

structure to the CsCl-type of crystal.[21]

2.2 Molecular Dynamics Method of Growth

In the present work, deposition of a Cu film on a (100) bcc Ta surface was simulated to mimic the growth of Cu interconnects on a Ta diffusion barrier, and deposition of a Cu_xTa_{1-x} alloy film ($0 \leq x \leq 1$) on a (111) fcc Cu substrate surface was simulated to explore possibilities of amorphization. The growth on (111) fcc Cu was chosen because the fcc crystal is the lowest energy phase of Cu and its (111) surface is the lowest energy surface. The lowest energy phase of bulk Ta is the tetragonal β phase. However, experiments indicated that for thin films, the β-Ta phase becomes metastable and would transform to a bcc (α-Ta) phase.[27] We therefore simulated the Cu growth on a (100) bcc Ta surface.

Sandia's parallel MD code LAMMPS[28] was used for our simulations. A computational substrate was first created by assigning positions of atoms according to crystal structure, equilibrium lattice constant, and crystallographic orientation of the substrate. The bcc Ta substrate includes 180 (200) planes in the x- direction, 5 (020) planes in the y- direction, and 180 (002) planes in the z- direction. The initial Ta substrate contains 40500 Ta atoms. An example of the substrate can be seen as the blue region in Fig. 2.4. Two fcc Cu substrates were used. One contains 232 $(2\bar{2}0)$ planes in the x- direction, 4 (111) planes in the y- direction, and 402 $(\bar{2}\bar{2}4)$ planes in the z- direction, and the other one contains 232 $(2\bar{2}0)$ planes in the x- direction, 13 (111) planes in the y- direction, and 402 $(\bar{2}\bar{2}4)$ planes in the z- direction. The two initial Cu substrates contain respectively 62176 and 202072 Cu atoms. The horizontal sizes of the Ta and Cu substrates are about the same, around 300×300 Å^2. However, the thickness of the two Cu substrates is about 8 and 27 Å respectively, compared with that of the Ta substrate of about 8 Å. The use of an additional thicker Cu substrate is to increase the distance between the Ta/Cu interface and the bottom boundary so that the mixing across the interface between deposited film and the Cu substrate can be studied.

With the substrates created, an initial substrate temperature was introduced by assigning velocities to atoms based upon a Boltzmann distribution. Periodic boundary conditions were used in the two horizontal (x- and z-) coordinate directions so that the simulated systems can be viewed as large planes in the x-z dimension. A free boundary condition was used in the vertical (y-) coordinate direction to allow for the surface growth. During simulations, adatoms were continuously injected to the top y- surface. The atom types were statistically assigned to match the desired composition of the vapor. The adatom injection frequency was assigned to match the desired growth rate. Newton's equations of motion were then used to solve for the positions of all system atoms as a function of time. A constant system volume condition was used so that the system size matched that of a simulated thick substrate.

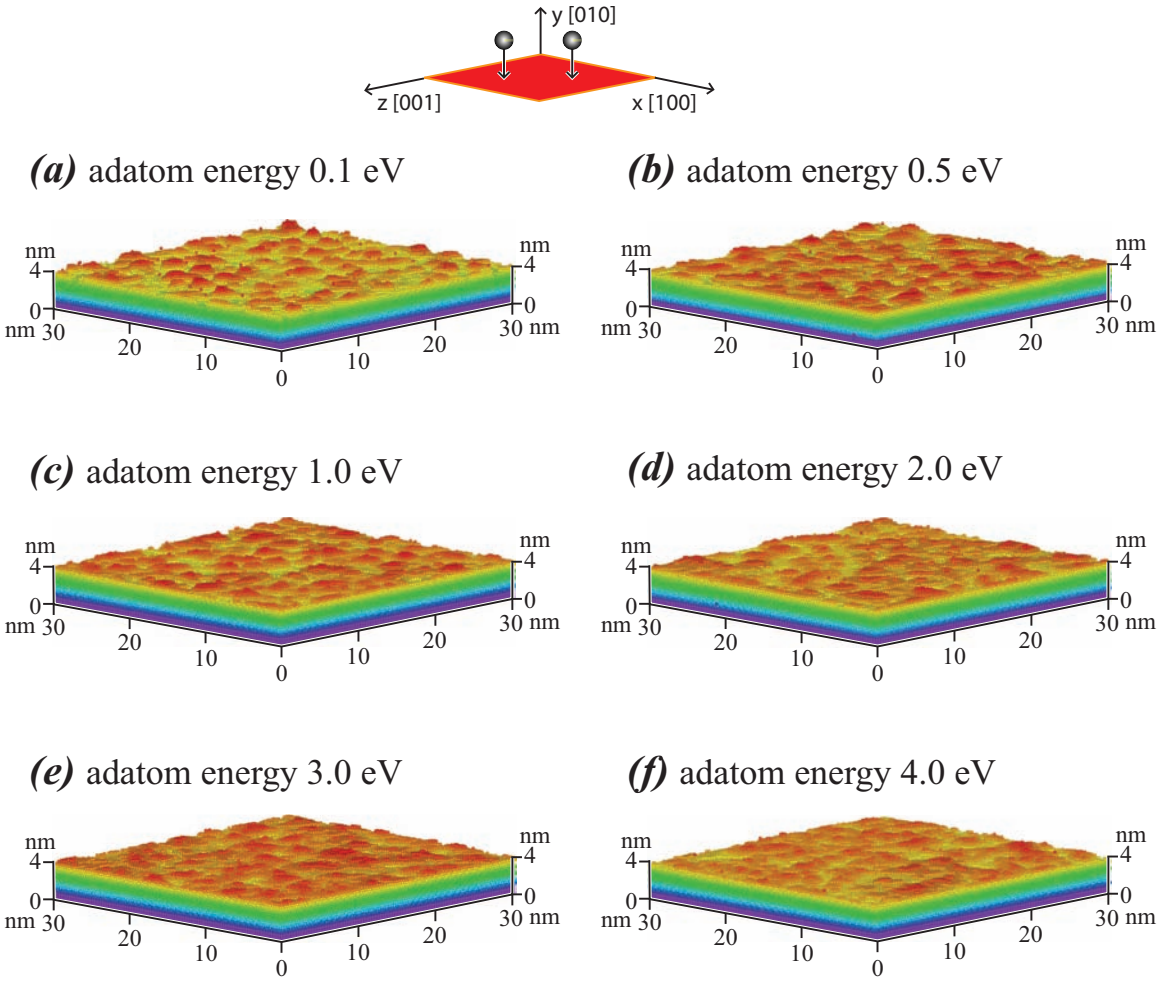

Figure 2.4. (Color) Cu-on-Ta surface morphology obtained from MD simulations. (a) adatom energy 0.1 eV; (b) adatom energy 0.5 eV; (c) adatom energy 1.0 eV; (d) adatom energy 2.0 eV; (e) adatom energy 3.0 eV; and (f) adatom energy 4.0 eV. Blue indicates Ta substrate, and other color scheme differentiates y coordinates.

To prevent the shift of the computational system due to the impact of the adatoms with the top surface, the positions of two bottom atomic plane of atoms were fixed during simulations. Due to the remote kinetic energy of adatoms and the latent heat release during adatom condensation, the system temperature arises. To mimic an isothermal growth condition, an intermediate region that is above the fixed region but several atomic planes below the surface was maintained at a desired substrate temperature using a Nose-Hoover algorithm.[29] This leaves a free surface zone that realistically captures various events induced during adatom impacts. It also naturally introduces a heat conduction zone through which the energy created at the surface during impacts is conducted to the temperature controlled region for dissipation. To minimize the change of heat conduction dimension, the temperature controlled region is expanded as the surface grows. To prevent the temperature controlled region from exceeding any surface boundary in the worst case scenario of forming a large surface roughness, the expansion rate of the temperature controlled region is adjusted to be smaller than the surface growth rate. For most simulations, about 30 Å thick films were grown. This corresponds roughly to 200,000 deposited atoms. All simulations were carried out at a room temperature and a deposition rate of about 0.5 nm/ns.

2.3 Experiments

Experimentally, 30 nm Cu on 30 nm Ta bilayer films were deposited on six inch silicon-silicon oxide wafers at room temperature using a biased target ion beam deposition (BTIBD) technique.[30] A base pressure of about 3×10^{-8} torr, a working pressure of about 8×10^{-4} torr, a depositing flux direction perpendicular to the growth surface, a fixed Ta sputtering energy of 400 eV, and various Cu sputtering energies between 400 eV and 1200 eV were used in all depositions. Depending on the depositing material and sputtering energy, the growth rate was found to roughly lie between 0.4×10^{-10} nm/ns and 1.5×10^{-10} nm/ns. X-ray diffraction measurement was used to characterize the film texture. A tapping mode atomic force microscopy (AFM) was used to analyze film surface morphology and the root mean square (RMS) surface roughness.

2.4 Growth of Cu on Ta

Synthesis of Cu interconnects is done by first depositing a thin Ta diffusion barrier layer on semiconductor devices and then depositing the Cu interconnecting layer on the Ta layer. Properties of the system are sensitive to the atomic structures of the Cu on Ta bilayer. For good performance, Cu on Ta interface must be chemically sharp and atomically uniform. High purity, high density, and high crystallinity are essential for the Cu layer to exhibit a high electrical conductivity. This also means that concentrations of defects such as surface roughness, growth islands, grain boundaries, voids, and dislocations must all be low. The control of surface roughness and growth

island density is critical because they can result in the formation of other defects such as grain boundaries, voids, and dislocations. Island coalescence is also a source for stress.[31] Here, the growth of Cu on Ta is first explored.

2.4.1 Observations of Atomic Structures as a Function of Adatom Energy

A series of molecular dynamics simulations were carried out to grow Cu films on Ta at different adatom energies between 0.1 eV and 5.0 eV. The resulting atomic images of the deposited films are shown in Fig. 2.4(a) - 2.4(f) at selected adatom energies, where the blue color is used to indicate the Ta substrate, and other color schemes are used to show the contrast for the y coordinate of the atoms so that the Cu film surface morphology can be clearly revealed. Fig. 2.4 indicates that as the adatom energy is increased, the surface roughness decreases. To verify this observation, a series of Cu films were experimentally grown on Ta using BTIBD technique at different sputtering energies between 400 eV and 1200 eV. According to previous analyses,[32, 33] the applied sputtering energy range roughly corresponds to the simulated adatom energy between 0.1 and 4.0 eV. AFM was used to measure the surface morphology of the deposited films. The results are shown in Fig. 2.5. Fig. 2.5 also shows that the Cu film surface roughness decreases with increasing adatom energy.

While both simulations and experiments show that the Cu surface roughness decreases with decreasing adatom energy, simulations were obtained at a deposition rate of about 0.5 nm/ns whereas experiments were done at a deposition rate of about 0.5×10^{-10} nm/ns. In addition, the horizontal dimension scale used in Fig. 2.4 is at least one order of magnitude smaller than that used in Fig. 2.5. To some extent, the effects of accelerated growth rate and short length scale cancel out. This is because surface atoms diffuse significantly less due to reduced diffusion time at accelerated deposition rates. It is to this perspective that MD results shown in Fig. 2.4 agree quite well with the AFM results shown in Fig. 2.5.

2.4.2 Surface Roughness as a Function of Adatom Energy

To quantify the effects of adatom energy on morphology, the root-mean-square (RMS) deviation of surface atoms from their mean height (y coordinate) was calculated from the atomic configurations of simulated Cu-on-Ta films as a function of adatom energy. The results of the calculations are shown in Fig. 2.6(a). Fig. 2.6(a) indicates that the RMS roughness of the Cu films decreases as adatom energy increases from 0.1 eV to 4.0 eV, with the rate of decrease higher at small adatom energies and lower at high adatom energies. RMS roughness was also measured experimentally from AFM samples. The results are shown in Fig. 2.6(b) as a function of sputtering energy. A similar trend to that shown in Fig. 2.6(a) is obtained. In particular,

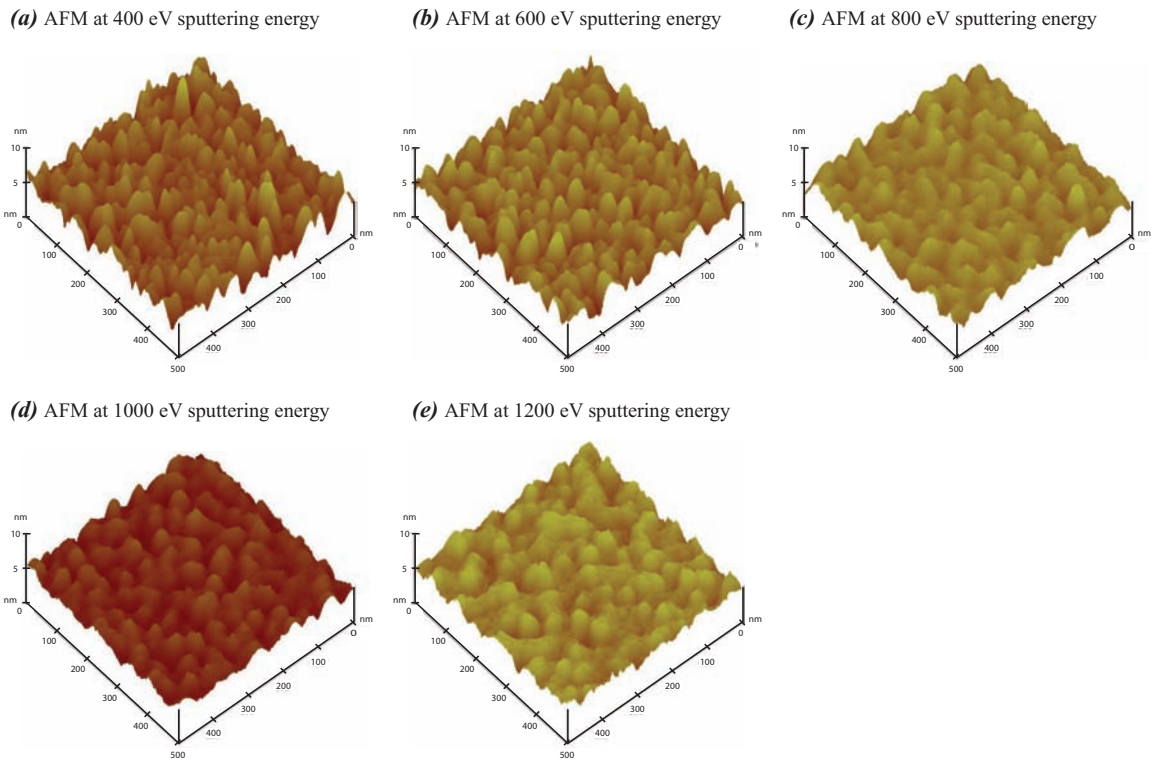

Figure 2.5. (Color) Cu-on-Ta surface morphology obtained from experiments. (a) sputtering energy 400 eV; (b) sputtering energy 600 eV; (c) sputtering 800 eV; (d) sputtering energy 1000 eV; and (e) sputtering energy 1200 eV.

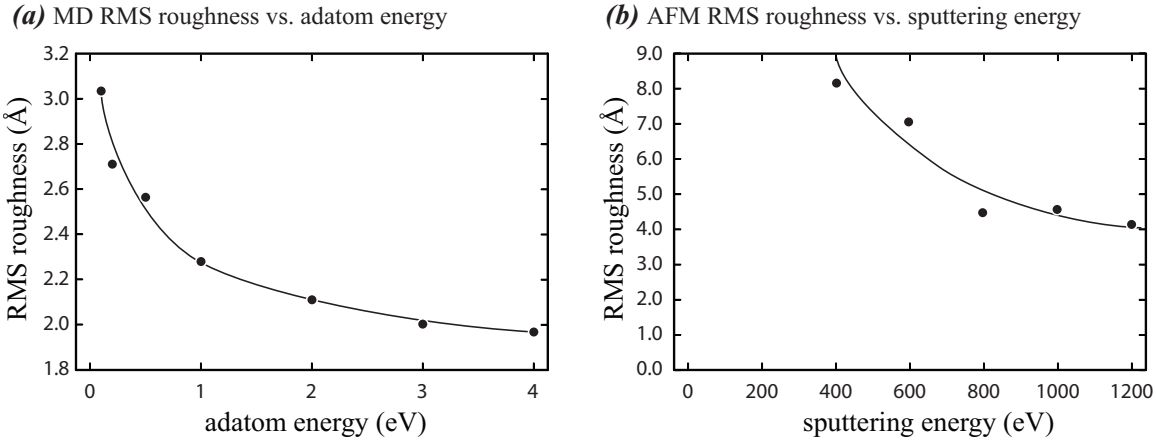

Figure 2.6. (a) MD roughness as a function of adatom energy; and (b) AFM roughness as a function of sputtering energy.

the surface roughness decreases with increasing sputtering energy, and the rate of decrease is higher at small sputtering energies and lower at high sputtering energies. Quantitatively, smaller roughness is obtained in MD than in experiments. This is consistent with a much smaller thickness of the simulated films. The adatom energy effect on surface roughness of growth films has been well studied.[23, 32] When an adatom with a higher energy impacts a surface with a local asperity, the impact is more likely to cause the collapse of the asperity, resulting in a flattening of the surface.

2.4.3 Grain Structure Observation

Examination of atomic images indicated that crystalline Cu films were obtained in all of our simulations. A detailed analysis was carried out to identify the atomic stacking of the Cu films. It was discovered that only the first atomic plane of Cu was somewhat epitaxial to the (100) bcc Ta substrate surface. Starting from the second plane, Cu quickly evolved to an fcc phase. In all simulations, Cu films grew in a [111] direction. Our subsequent XRD experiments using BTIBD samples verified that Cu films deposited on Ta were fcc crystals with a very strong [111] texture.

Our test simulations indicated that when relatively small horizontal dimensions (e.g., 50 Å) were used, the simulated Cu films usually contained only one grain in the simulated film area. Small systems are not realistic even when the use of periodic boundary condition removes the surfaces in the x- and z- directions. This is because the periodic boundary condition imposes constraints on the motion of atoms near cell boundaries. For our systems that contained about 300 Å horizontal dimension, polycrystalline Cu films were observed in all of our simulations of Cu growth on a single crystalline Ta. The grain structure was found to be relatively insensitive to adatom energy. As an example, Fig. 2.7 shows four consecutive atomic planes inside a Cu film deposited on Ta at an adatom energy of 4.0 eV, where four different colors are used to distinguish y coordinates (planes). Clearly, the film exhibits two grains, one in orientation marked as "A" and the other in orientation marked as "B". Both grains have fcc stacking with a (111) surface. One interesting discovery is that all of our simulated Cu films contained only the two orientations shown in Fig. 2.7.

Further examinations of grain structures were carried out. Fig. 2.8 shows an example of a Cu film deposited at 0.1 eV, where several consecutive atomic planes inside the Cu film are viewed at a tilted angle from top with different colors showing the y coordinate of the atoms. It can be seen that multiple grains were formed. These multiple grains appeared to result in the formation of grain boundary junctions where three "grain" boundaries meet. Normally grain boundary junctions require that the three joining boundaries are between grains with different orientations with respect to each other. As pointed out above, only two orientations were observed in the Cu films. Careful examination of Fig. 2.8 indicates that only two boundaries at the grain boundary junctions are the regular orientational boundaries that separate grains with different orientations. The remaining boundary, however, is a translational boundary that

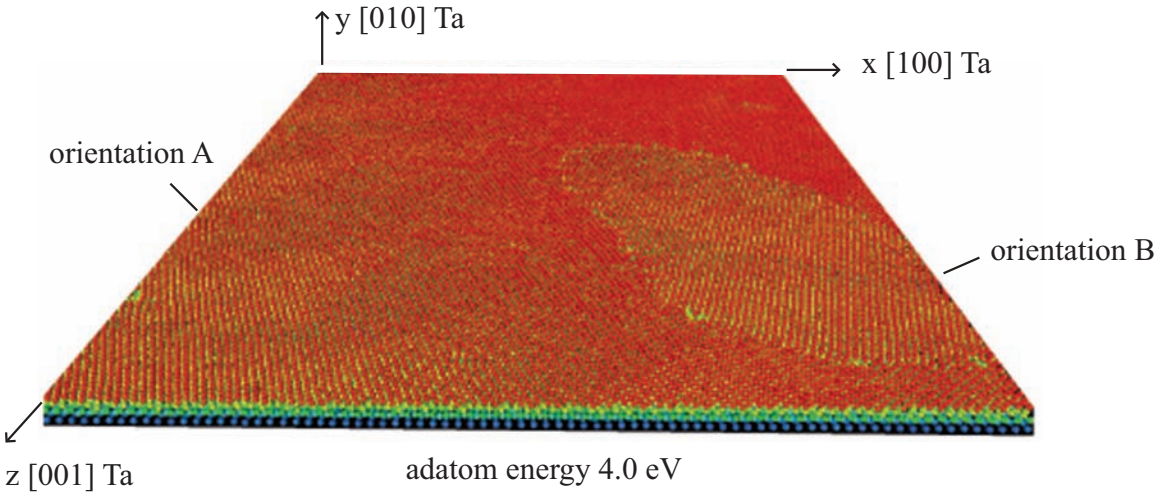

Figure 2.7. (Color) Four consecutive atomic planes inside a Cu film deposited on Ta at 4.0 eV adatom energy.

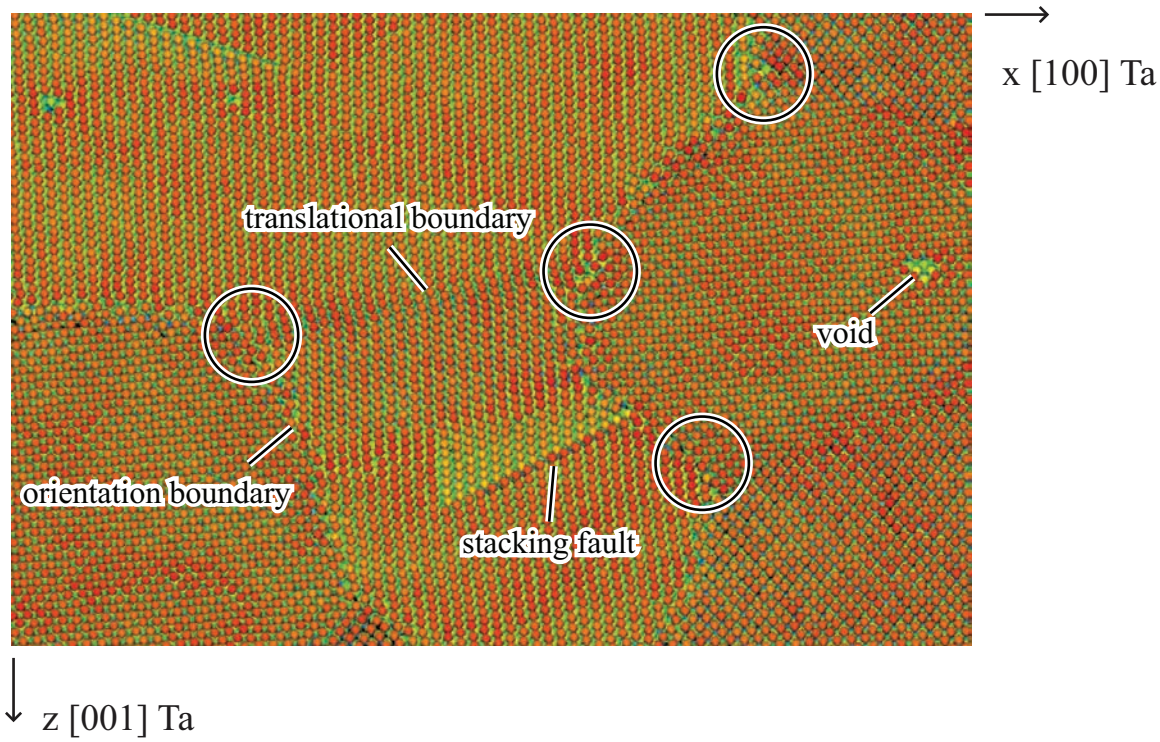

Figure 2.8. (Color) Tilted top view of a few consecutive atomic planes inside a Cu film deposited on Ta at 0.1 eV adatom energy. Circles mark grain boundary junctions where three grain boundaries meet.

separates "two" grains with the same orientation except that they are translationally shifted with respect to each other. As a result, such a boundary originated from a dislocation. In addition to grain structures, Fig. 2.8 reveals the presence of other defects such as voids and stacking faults (bounded by dislocations). The change of color within the stacking fault bands suggests that these stacking fault planes are tilted from the surface plane. It should be noted that the translational boundary, which is essentially a dislocation, should also cause stacking fault. In this case, however, the stacking fault plane coincides with the surface plane.

Fig. 2.7 and 2.8 reveal the grain structures that form during accelerated deposition of Cu on (010) bcc Ta. It is not clear how stable these grain structures are and if they can maintain in the films when the growth rate is significantly decreased. To address these issues, the time evolution of grain configurations was studied. Fig. 2.9 examines a Cu film deposited at an adatom energy of 0.1 eV, where Fig. 2.9(a) is a three dimensional view of the film, Figs. 2.9(b) - 2.9(d) are time evolution snapshots of plan view of a narrow layer of material inside the Cu film as indicated in Fig. 2.9(a). It can be seen from Figs. 2.9(b) - 2.9(d) that little change in the grain structure occurred during a 2031 - 2995 ps time period. As molecular dynamics simulations at finite temperatures are fairly effective in finding low energy configurations, the results shown in Fig. 2.9 verify that the observed grain structures were fairly stable. It is not surprising that the orientational grain boundary is stable at least when the grain sizes are not too small because the migration of grain boundaries requires significant reconstruction of atoms. The translational grain boundary is also seen to be stable. Furthermore, we noticed that very thin films were usually absent of translational grain boundaries and only after the films grew beyond a critical thickness then the translational boundaries (dislocations) were nucleated within an otherwise relatively perfect grain. This is similar to the formation of misfit dislocations to release the misfit strain energy when the film thickness exceeds a critical value.[34, 35] Because the translational boundary is likely to correspond to a lower misfit strain energy, it is therefore stable.

2.4.4 Grain Structure Formation Mechanisms

The results discussed above showed mainly two grain phenomena: (a) the formation of grains with two characteristic orientations and (b) the formation of stable translational boundaries (dislocations). Atomistic simulations allow us to explore fundamental mechanisms for these two phenomena. As a representative example, a Cu film deposited at an adatom energy of 3.0 eV is examined in Fig. 2.10. In Fig. 2.10(a), a plan view of three consecutive atomic planes inside the Cu film is displayed using different colors to distinguish different planes. A periodic band structure is seen. In the relatively dark bands, atoms with all three different colors are shown, indicating local a ABCABC... hexagonal stacking in the [111] fcc (growth) direction. In the relatively bright bands, only atoms with two different colors are shown, indicating a local ABAB... stacking in the [111] fcc direction. As a result, these bands

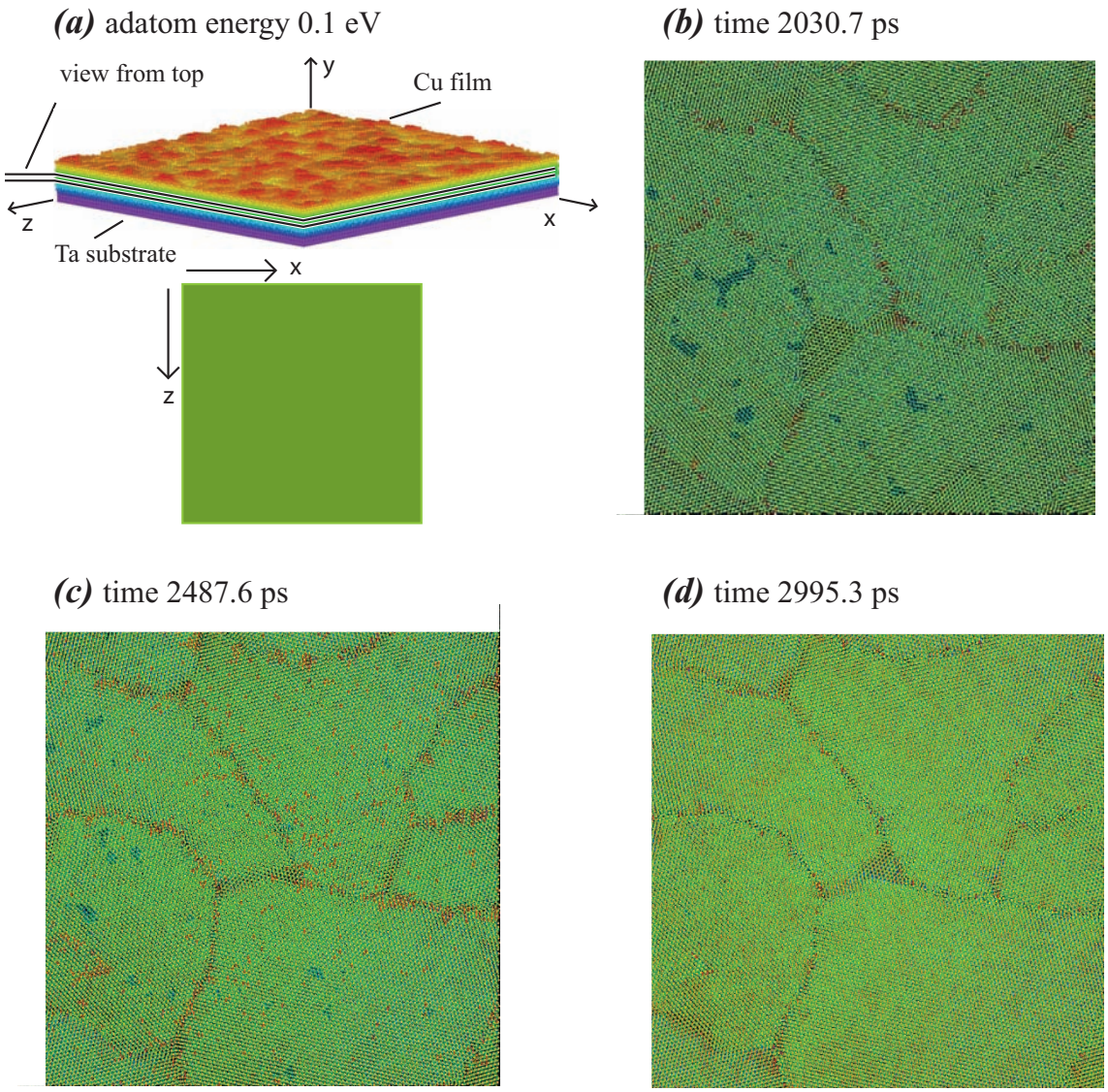

Figure 2.9. (Color) Grain structure formation during deposition. (a) three-dimensional geometry; (b) plan view at 2030.7 ps; (c) plan view at 2487.6 ps; and (d) plan view at 2995.3 ps.

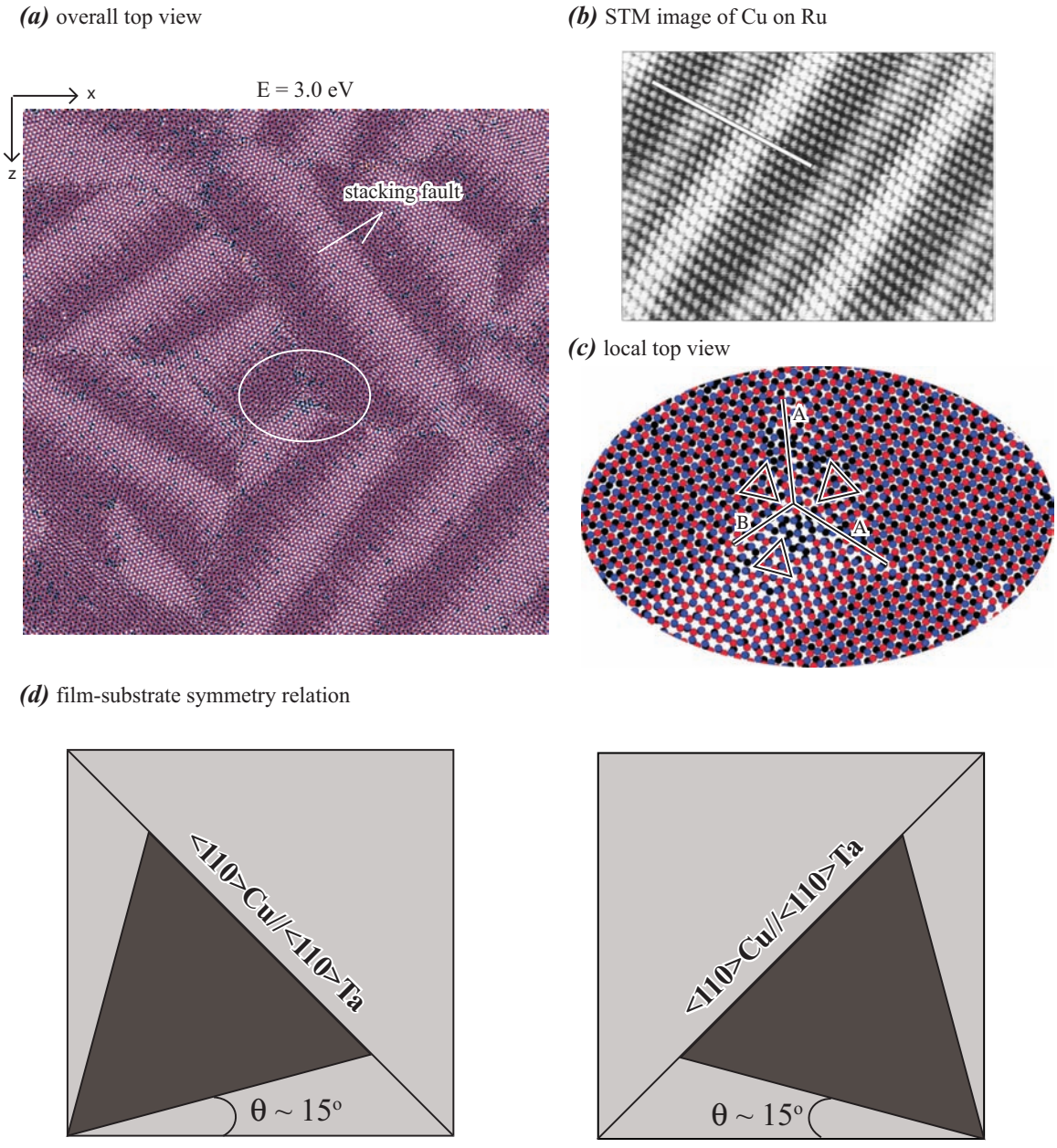

Figure 2.10. (Color) Grain orientation. (a) overall top view of three deposited Cu atomic planes near the Cu-on-Ta interface; (b) high resolution scanning tunneling microscopy (STM) image of a Cu film deposited on local (0001) Ru surface; (c) local view [circular region in (a)] of a tri-grain boundary junction; and (d) film-substrate symmetry relation, where dark area shows {010} bcc Ta symmetry, light area shows {111} fcc Cu symmetry.

are periodic stacking faults on the surface plane. In fcc Cu, these stacking faults are separated by partial dislocations with Burgers vectors $\frac{1}{6}\langle 112\rangle$a, where a is the lattice constant of Cu. It can be seen that these partial dislocations are not only present at the translational "grain" boundaries, but also inside each grain. High resolution scanning tunneling microscopy experiments revealed similar periodic stacking faults on a Cu-on-(0001)Ru surface, Fig. 2.10(b),[36] which has been elucidated using simulations.[37]

In order to examine the structure in more details, the circular region marked in Fig. 2.10(a) is magnified and is examined in Fig. 2.10(c). The orientation of a grain can be visually represented by a triangle connecting, for instance, the six red atoms on the hexagonal (111) surface. It can be seen that the two grains at the left side have the same orientations as they are represented by the same lay-out of triangles, whereas the grain at the right has a different orientation as it is represented by a different lay-out of triangle. As a result, boundary "A" between left and right grains are the orientational boundary and boundary "B" between the two left grains is the translational boundary. Furthermore, we superimpose the two different orientations of the triangle identified in Fig. 2.10(c) over the square symmetry of the [010] bcc Ta, and display the result in Fig. 2.10(d), where the light shaded squares represent the (010) symmetry of the bcc Ta, and the dark shaded triangles represent the (111) symmetry of the fcc Cu. We can see that one side of the triangle, which is a $\langle 110\rangle$ fcc Cu direction, is always parallel to the diagonal of the square, which is a $\langle 110\rangle$ bcc Ta direction. The parallel relationship between $\langle 110\rangle$ fcc Cu and $\langle 110\rangle$ bcc Ta is not surprising as both directions are close packed when projected on the surface plane. It can now be seen from Fig. 2.10(d) that because there are only two diagonal directions of the square, there are only two orientations for the triangles (therefore, grains). As the two diagonals are perpendicular, the two Cu grain orientations are related by a 90° rotation.

During growth simulations using small horizontal dimensions, new grains are nucleated at locations close to existing grains. This creates high energy configurations and new grains are likely to be eliminated (eaten) by existing grains at the nucleation stage. As a result, simulated films often exhibited a single crystal. During growth of the Cu films on a large plane of Ta surface, Cu grains are nucleated at random locations. The probabilities of forming either of the two orientations are exactly the same when the nucleated gains are far apart and therefore independent. When these grains grow to meet each other, the grain sizes are already big and therefore, relatively stable orientational boundaries are formed. This explains why two and only two grain orientations were observed in all simulations.

The observed periodic stacking faults / partial dislocations were caused by lattice mismatch. Unlike the misfit dislocations that accommodate the size difference between the two layers,[34, 35] the observed misfit dislocations must accommodate both size and structure differences between bcc Ta and fcc Cu. The origin of the observed misfit dislocation configurations are explored in Fig. 2.11, where in Fig. 2.11(a), the

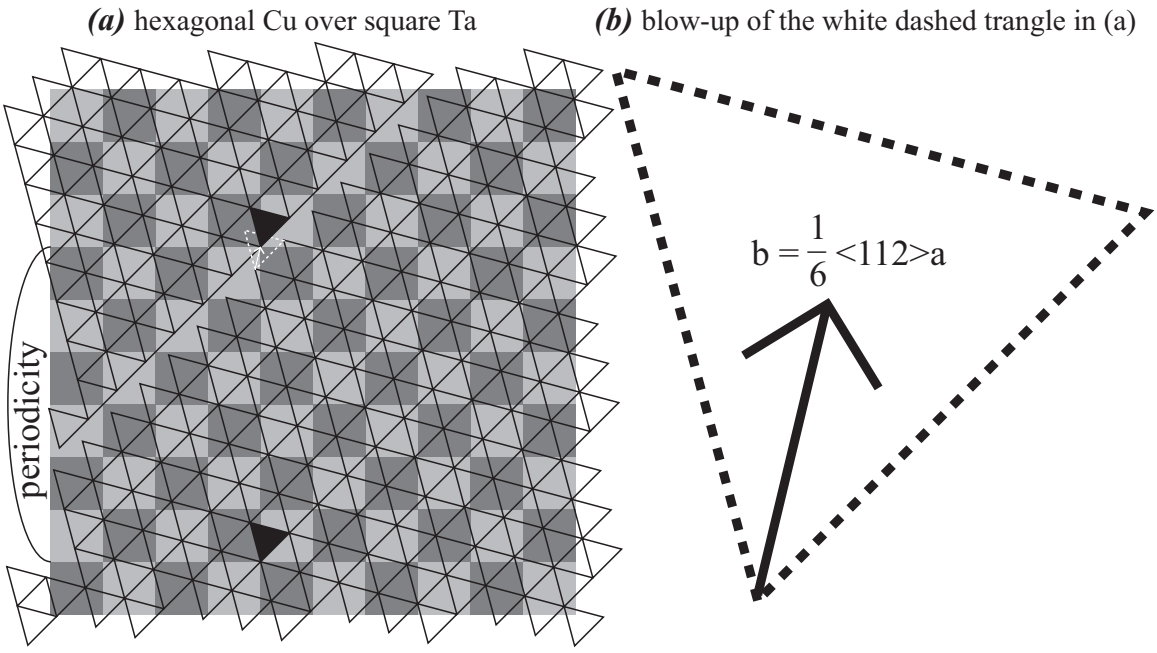

Figure 2.11. Origin of misfit dislocations. (a) stacking geometry of a (111) fcc Cu grain on the (100) bcc Ta substrate; and (b) blow-up of the white dashed triangle shown in (a).

alternate dark and light shaded squares represent a (100) bcc Ta surface, and the triangles represent a (111) Cu plane in the orientation of the two left grains shown in Fig. 2.10(c), whereas in Fig. 2.11(b), a blow-up of the white dashed triangle in Fig. 2.11(a) is shown. In the figure, the relative size of the triangles with respect to that of the squares matches the real material lattice constants so that misfit is reflected. To examine the periodicity of the (111) Cu on the (100) Ta, two of the triangles are marked black in Fig. 2.11(a) and the lower black triangle is aligned (corner on corner) with the underlying square. It can be seen from Fig. 2.11(a) that a perfect (111) Cu on (100) Ta does not have a short range periodicity along the vertical direction. As a result, the misfit energy becomes large as the feature size increases. However, if the upper-left part of the (111) plane is shifted with respect to the lower-right part of the plane by a vector marked inside the white dashed triangle, a periodicity of a length of six squares is created. Fig. 2.11(b) indicates that this shift vector corresponds to the Burgers vector of a partial dislocation $\frac{1}{6}\langle 112\rangle$a of the Cu lattice. As a result, the long range misfit strain energy is well released by the creation of the low energy partial dislocations. The dislocation line direction seen in Fig. 2.11(a) matches the stacking fault band direction shown in Fig. 2.10(c), and the periodicity identified in Fig. 2.11(a) gives a stacking fault band width slightly shorter than that seen in Fig. 2.10(c). Because both dislocations and stacking faults introduce additional energies, it is expected that the actual stacking fault band width (misfit dislocation separation distance) is longer than the one shown in Fig. 2.11(a).

Fig. 2.11 identifies only one dislocation (line and Burgers vector) characteristic of one grain orientation. Because there are two perpendicular grain orientations, two perpendicular arrays of stacking fault bands / dislocations are seen in Fig. 2.10(a), with each array coming from one grain orientation.

The analysis above indicates that the formation of polycrystalline Cu films, translational boundaries, and periodic stacking fault bands / dislocations are all low energy configurations. They are therefore stable. Because they are not metastable defects created under kinetically constrained conditions, they are difficult to eliminate by controlling kinetic growth conditions or by use of high quality single crystalline substrates.

2.5 Growth of Cu_xTa_{1-x} on Cu

The diffusion barrier application requires only the growth of Cu on Ta. Simulations of Ta on Cu are motivated by the experimental discovery that alternate electron beam deposition of Cu and Ta under Ar ion assistance can produce amorphous films around a film composition of $Cu_{0.3}Ta_{0.7}$.[14] In the experiment, the film composition was controlled by the relative thickness of the deposited Cu and Ta layers. This means that extensive mixing occurred either during deposition of Cu on Ta or Ta on Cu. This mixing can be caused by high energy Ar impacts.[38, 39, 40, 41] Simulations discussed above shows that at the absence of Ar assistance, little mixing occurs during growth of Cu on Ta. It is not clear if mixing can occur during growth of Ta on Cu. Our bulk simulation results shown in Figs. 2.1 and 2.2 indicated that crystalline metals are readily formed when the material is either Cu (or Cu-rich) or Ta (or Ta-rich). In these cases, crystallization is difficult to inhibit as the kinetics is extremely fast in metals. When mixing occurs, especially when the Cu and Ta compositions in the alloy (solid solution) are comparable, an amorphous phase is likely to form because the lattice mismatch strain energy is so large that it cannot be fully released by any crystal-maintaining density of defects such as misfit dislocations. This effect is predicted in Figs. 2.1(c) and 2.2. It is therefore critical to create highly mixed region and inhibit separation to Cu-rich and Ta- rich phases in order to initiate amorphization.

Previous studies [23, 25, 32] have indicated that when the underlying surface is composed of atoms with a lower cohesive energy, a larger lattice spacing, and a lower surface energy with respect to the depositing atoms, the depositing atoms are more likely to penetrate the underlying surface through the lattice interstices and the underlying atoms are more likely to be exchanged to the surface to release both surface tension and surface energy. A continuous surface segregation of the underlying atoms to the surface then causes them to be mixed into the overlying deposited layer. Although the radius of Cu is smaller than that of Ta, the cohesive energy of Cu, -3.54 eV/atom, is significantly smaller in magnitude (less negative) than that of Ta, -8.09 eV/atom. This suggests that Cu atoms are likely to segregate to the Ta surface to

release the high surface energy (which is caused by the broken Ta bonds), and that the depositing Ta atoms are likely to penetrate a weakly bonded Cu surface to cause the Cu-Ta exchange. This observation suggests that there could be a significant mixing across the Ta-on-Cu interface. If this is the case, it provides a new avenue for the synthesis of amorphous films. An alternative approach that offers control of film composition is to deposit Cu_xTa_{1-x} films on Cu, with x somewhere between zero and one. Considering that surface segregation and phase separation may occur during the growth, it is not clear how the film composition relates to the vapor phase composition. The atomic assembly mechanisms during growth of Ta on Cu can therefore provide useful insights that lead to better design concepts. Here we explore the formation of amorphous films by simulating the growth of Cu_xTa_{1-x} films on Cu using a variety of compositions x.

2.5.1 Atomic Structure Observations

A series of MD simulations were carried out to grow Cu_xTa_{1-x} films on Cu at a constant adatom energy of 3.0 eV and various compositions of x, $0 \leq x \leq 1$. Here the composition x refers to the vapor composition and the actual film composition is likely to be different considering that Cu atoms in the underlying Cu substrate may be mixed into the deposited film. Examples of atomic configurations of deposited films are shown in Fig. 2.12, where plan views of a small area of three consecutive atomic planes inside the deposited films are shown in Figs. 2.12(a) - 2.12(d) for four selected film compositions x = 0.0, 0.2, 0.4, and 1.0. It can be seen that at x = 0.0, Fig. 2.12(a), the growth of Ta on Cu resulted in a film that in most part is composed of crystalline grains. Following the same analysis above, we found that all the Ta grains have a (110) plane parallel to the (111) Cu substrate surface. The grain orientation can be represented by a rectangle connecting the eight red (orange) atoms. The short side of the rectangle is parallel to the $\langle 100 \rangle$ bcc Ta direction, and the long side of the rectangle is parallel to the $\langle 110 \rangle$ bcc Ta direction. We further found that for all of the Ta grains, one of the $\langle 100 \rangle$ bcc Ta direction is parallel to one of the $\langle 110 \rangle$ fcc Cu direction. Because on the hexagonal Cu surface, there are only three nonequivalent $\langle 110 \rangle$ directions. As a result, only three Ta grain orientations were discovered in all of our simulations. An additional finding in Fig. 2.12(a) is that the regions between grains are disordered, which is characteristic of an amorphous phase. The width of these disordered regions increased toward the Ta-on-Cu interface. These observations indicate that the amorphization is driven by a combination of lattice mismatch across the Ta/Cu interface and the grain boundaries.

Fig. 2.12(b) shows that the structure of the $Cu_{0.2}Ta_{0.8}$ film is very similar to that of the Ta film. However, when the film composition was increased to x = 0.4, Fig. 2.12(c), the area of disordered regions increased significantly. These regions essentially formed a considerable volume fraction of an amorphous structure. Finally, when the composition is x = 1, the growth of Cu on Cu resulted in the formation of a relatively perfect fcc Cu single crystalline film on Cu substrate, Fig. 2.12(d).

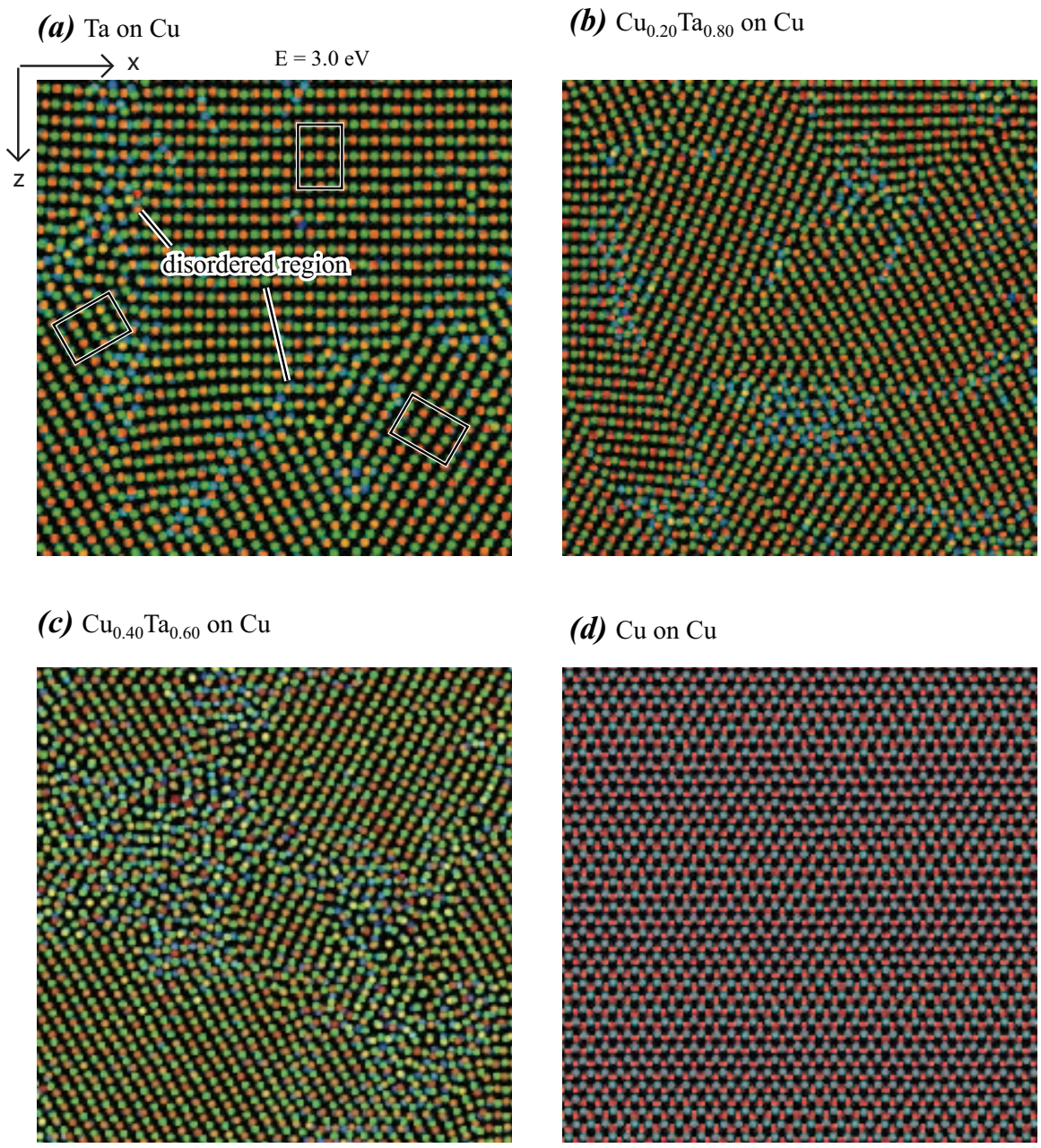

Figure 2.12. (Color) Top views of the first three atomic planes of Cu_xTa_{1-x} films deposited on Cu at an adatom energy of 3.0 eV. (a) Ta on Cu; (b) $Cu_{0.2}Ta_{0.8}$ on Cu; (c) $Cu_{0.4}Ta_{0.6}$ on Cu; and (d) Cu on Cu.

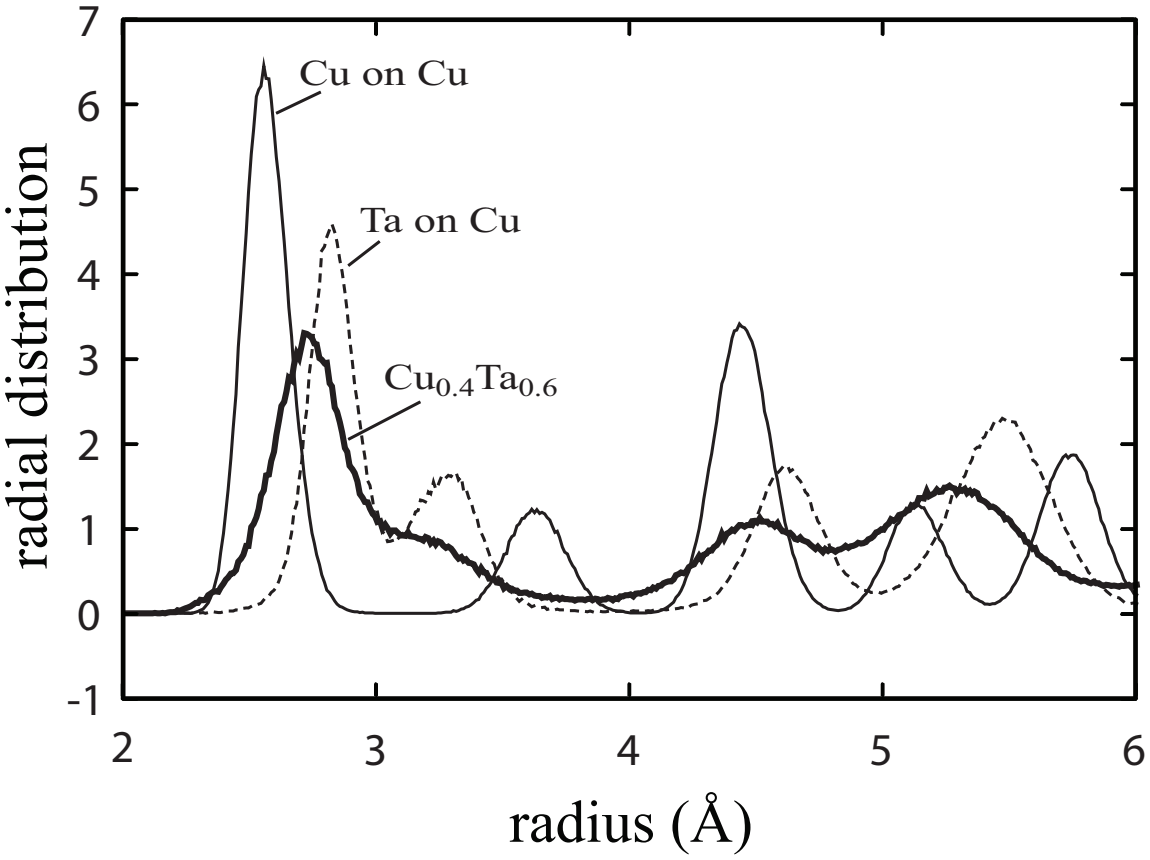

Figure 2.13. Radial distribution functions for selected films.

To verify the observation from Fig. 2.12, radial distribution functions were calculated for films deposited at different compositions. Selected results are shown in Fig. 2.13. Comparison between Figs. 2.2 and 2.13 indicates that the Cu films on Cu exhibited an fcc crystalline structure, the Ta films on Cu is dominated by a bcc crystalline structure, and the $Cu_{0.4}Ta_{0.6}$ films on Cu is dominated by an amorphous structure.

2.5.2 Interlayer Mixing

Amorphization in binary metal atoms is believed to be driven mainly by heat of mixing, atomic size difference, and crystal structure difference.[15, 42, 43, 44] When the heat of mixing is high, the system tends to be separated to two elemental phases. Only when the heat of mixing is low, a highly mixed solid solution forms. Amorphization then occurs if significant atomic size and crystal structure difference result in significant energy in crystalline structures. The use of vapor deposition offers unique means to create mixed film composition than other bulk synthesis methods.

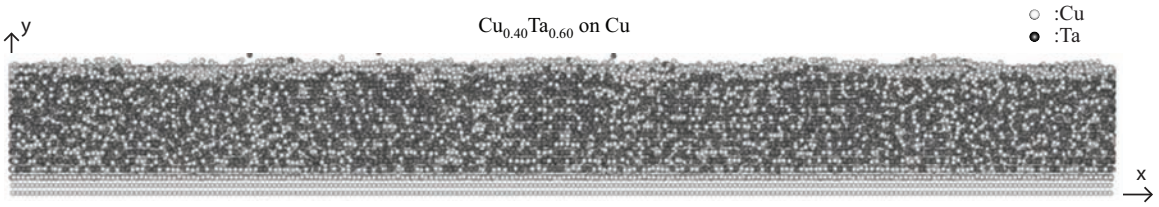

Figure 2.14. Front view of a $Cu_{0.4}Ta_{0.6}$ film deposited on Cu at an adatom energy of 3.0 eV.

Interlayer mixing created during vapor deposition is hence important to understand.

The film compositions marked in Figs. 2.12 and 2.13 are the vapor compositions used in simulations. Due to effects such as surface segregation, the actual local composition in the film differs from the vapor composition. Obviously, amorphization is a result of local composition in the film. To show possible composition distribution expected in the films, the front view of a $Cu_{0.4}Ta_{0.6}$ film deposited on Cu at an adatom energy of 3.0 eV is shown in Fig. 2.14, where darker balls represent Ta atoms and lighter balls are Cu atoms. It can be seen that Cu has a strong surface segregation effect, consistent with its lower cohesive and surface energies. Due to this surface segregation, the Cu composition near the surface is expected to be higher than that deep inside the film.

The key to create amorphous structure is to induce mixing. Due to the Cu surface segregation effect, Cu tends to be mixed in the later deposited Ta films. As a result, depositing Ta on Cu, in conjunction with Ar ion assistance to induce atomic exchange at the surface, helps create a mixed interface. This accounts for why an alternate deposition of Cu and Ta can be used to experimentally synthesize thicker amorphous films. On the other hand, directly depositing Cu_xTa_{1-x} alloy films offers a useful means to better control film composition. However, due to Cu surface segregation, Cu composition tends to increase as the film thickness increases when using this approach. In addition, phase separation may occur. Experimental efforts are required to identify the growth of amorphous films using the Cu_xTa_{1-x} alloy vapor flux.

2.6 Conclusions

Molecular dynamics simulations and selected microscopic experiments have been performed to study the growth of fcc Cu films on (010) bcc Ta substrate and Cu_xTa_{1-x} alloy films on (111) fcc Cu substrate. The following results have been obtained.

(a) The roughness of Cu films deposited on Ta decreases as adatom energy is increased due to an impact induced flattening mechanism.

(b) Cu deposited on (010) Ta always forms fcc polycrystalline films with a (111) texture. The crystalline grains only have two orientations and are separated by either orientational boundaries or translational boundaries (dislocations). Formation of two crystal orientations is due to crystalline symmetry between Cu film and Ta substrate. Formation of translational boundaries is due to misfit dislocations.

(c) A characteristic array of periodic stacking fault bands / misfit dislocations is formed within each Cu grain orientation to release misfit strain energies. Two grain orientations then result in two perpendicular arrays of stacking fault bands / misfit dislocations in polycrystalline Cu films.

(d) Cu has a strong surface segregation effect when Ta is deposited on Cu. This causes underlying Cu to float up and mix in subsequently deposited Ta or Cu_xTa_{1-x} films. As a result, the Cu composition in the Cu_xTa_{1-x} layer is always higher than vapor composition.

(e) Amorphous phase can form when the Cu and Ta compositions in the deposited films are comparable. This can be achieved by either alternatively depositing Cu and Ta with inert gas ion assistance, or directly depositing Cu_xTa_{1-x} alloy films with controlled vapor composition and highly kinetically constrained growth conditions, or combination of both.

Chapter 3

Simplified Computational Methods for the Study of Diffusional Problems

The study of kinetic processes in materials has been immensely aided by the development of mathematical models and computational methods that retain the consequences of fundamental atomic scale processes in predictions of microstructural evolution over physically realistic time scales.[45] Continuum models and kinetic Monte Carlo methods have been used to do this. The most widely used continuum approaches coarse grain the atomic phenomena into diffusion and chemical reaction processes and set up diffusion partial differential equations to deduce composition fields and second phase distributions. Numerical methods must be used to solve these equations. For systems involving the random diffusion of multiple elements, multiple second order parabolic partial differential equations (e.g., Fick′s law) need to be simultaneously solved.[46] For non-random diffusion, higher order partial differential equations (e.g., Cahn Hilliard′s equations [47, 48]) are necessary. On curved surfaces, diffusion is also a function of local surface curvature, which increases the order of the partial differential equations.[49] The solution of these equations then becomes much more difficult because of the increase in the order of the partial differential equations. To study kinetic processes on surfaces, the diffusion equations may need to be integrated into other methods such as the level set method developed by Sethian.[50]

Continuum methods require a material structure to be represented by continuous functions. This introduces constraints upon their use for vapor deposition simulations. During deposition, adatoms randomly condense on the surface. This means that regions on the local surface frequently advance within very short times leading to non-continuous derivatives of the surface profile and a divergence of the numerical calculations.

Kinetic Monte Carlo (kMC) methods are suited for studies of the evolution of significant atomic structures (involving millions of atoms). They enable a simulation of the individual atomic jumps (based on a prior calculation of their relative jump frequencies) of all atoms in the system over physically meaningful periods of time.[51, 52]

The kMC method has limitations for some problems. Atom jump frequencies exponentially increase with temperature according to the Arrhenius equation. Because each atom jump is simulated, the time that can be analyzed during a kMC simulation decreases with jump frequency. Furthermore, some systems can have very high jump frequencies, even at ambient temperatures. For instance, the diffusion of a single copper atom on a (111) copper terrace has a diffusion activation energy barrier of only 0.026 eV.[53] This leads to a jump frequency of 7×10^{11}/s at 300K. If such a single adatom falls on a (111) surface during a crystal growth simulation, most of the computational resources will be allocated to a tracking of the random walk of this atom, and relatively little will be learnt about the overall structural evolution. In these scenarios, the usefulness and efficiency of the kMC simulations can be significantly reduced. In the limit, as the jump frequency approaches atom vibration frequency, kMC calculations must be carried out with a jump time scale that approaches the surface atom vibration period. At this point, the computational efficiency of kMC approaches that of molecular dynamics methods.

Here we investigate a diffusional Monte Carlo (dMC) approach that may permit an alternative means for the study of material transport processes. Unlike kMC methods that simulate each atom jump, the dMC method self-consistently selects the net diffusion effect of all of atom jumps during the simulated time. As a result, the approach is well suited for slow processes. The simulation efficiency is found to depend only weakly upon problem space conditions such as temperature and diffusional activation energy barriers. To develop the approach, we begin with a discussion of atomistic diffusion theory and use this to define continuum diffusion equations for random and non-random diffusional processes. The dMC approach is then introduced and investigated in the context of composition-driven random diffusion processes in one-, two-, and three-dimensions including the dissolution of a spinodal structure (reverse spinodal decomposition). We also demonstrate that the non-random diffusion theory can be applied to predict spinodal decompositions.[47]

3.1 Atomistic Theory for Random Diffusion

To compare the results of atomistic and continuum simulations, atom jumps need to be related to continuum diffusion equations. The simplest case to consider is the situation where each atom randomly diffuses in a material. An illustration of the atom jumps between adjacent atomic planes during a random diffusion process is shown in Fig. 3.1(a), where the two thick solid lines represent the two adjacent atomic planes separated by a spacing, a, and the thick solid curve is the energy variation when an atom jumps from one plane to the other. Random diffusion occurs when the energy curve is symmetric with equal minimum energies at both the left and the right atom planes and when this is independent of local composition. Under these conditions, any given atom would have an equal probability of occupying a lattice site in either the left or the right plane. It can be seen from Fig. 3.1(a) that the energy barriers

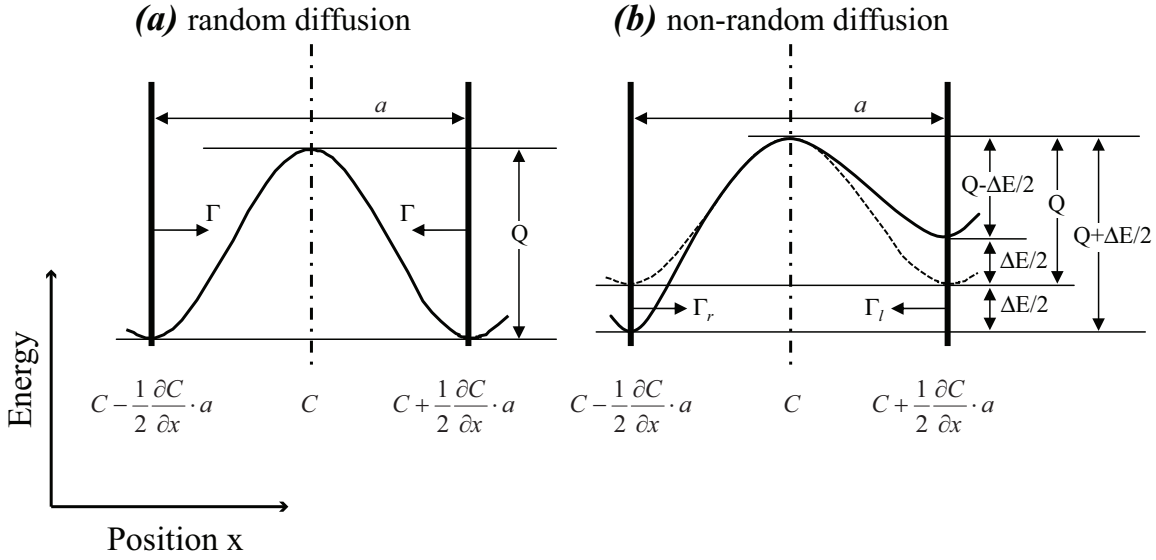

Figure 3.1. Atom jumps between adjacent planes. (a) random diffusion; and (b) non-random diffusion.

to the left and to the right are equal and so they are both represented by a value, Q. At a given temperature, the energy barrier defines the jump frequency through the Arrhenius equation. As a result, the jump frequencies to the left and to the right are also equal and are represented by a single value, Γ.

If it is assumed that a volume unit at the center (dash-dot) line between the two planes has an average composition (atoms per volume) of C, and an average composition gradient of $\frac{\partial C}{\partial x}$, to first order, the compositions at the left and the right planes can be written as $C - \frac{1}{2}\frac{\partial C}{\partial x} \cdot a$ and $C + \frac{1}{2}\frac{\partial C}{\partial x} \cdot a$ respectively. The net flux of atoms, J, flowing from the left to the right plane, can be written as

$$J = \left(C - \frac{1}{2}\frac{\partial C}{\partial x} \cdot a\right) \cdot a \cdot \Gamma - \left(C + \frac{1}{2}\frac{\partial C}{\partial x} \cdot a\right) \cdot a \cdot \Gamma = -\Gamma \cdot a^2 \cdot \frac{\partial C}{\partial x} = -D\frac{\partial C}{\partial x} \quad (3.1)$$

where $D = \Gamma \cdot a^2$. It can be seen that the net flow of atoms is driven by composition gradient as individual atoms have an equal probability to jump in either direction. Eq. (3.1) is essentially Fick′s first law of diffusion with D being the diffusivity coefficient.

A partial differential equation can be constructed to solve for the composition profile as a function of time. Again consider a small volume unit at the center line shown in Fig. 3.1. If the flux flowing into the unit volume through its left hand side equals the flux flowing out of its right side, then no composition change would occur within the unit. Because the composition change always results from differential fluxes, the rate of composition change can be written as

$$\frac{\partial C}{\partial t} = -\frac{\partial J}{\partial x} \quad (3.2)$$

Substituting Eq. (3.1) into Eq. (3.2) gives Fick′s second law of diffusion,

$$\frac{\partial C}{\partial t} = \Gamma \cdot a^2 \cdot \frac{\partial^2 C}{\partial x^2} \tag{3.3}$$

3.2 Atomistic Theory for Non-Random Diffusion

When the energy changes with lattice site occupancy, atoms preferentially occupy sites that reduce the system energy. The atom flow then depends not only on the composition difference, but also on the energy difference. If a significant energy driving force is present, atoms can flow from a low composition region to a high composition region, resulting in uphill diffusion. Such a scenario is considered in Fig. 3.1(b), where the minimum energy at locations to the right is higher than that to the left by ΔE. For comparison, we superimpose the symmetric energy curve in Fig. 3.1(b) using a dashed line. In the simplest case, the minimum energy is shifted by $\Delta E/2$ to the right and by -$\Delta E/2$ to the left from the symmetric case. It can be seen that the energy barrier for atoms to jump from the right to the left plane, Q_l = Q - $\Delta E/2$, is lower than that for atoms to jump from the left to the right plane, Q_r = Q + $\Delta E/2$. As a result, the frequency for atoms to jump from the right to the left, Γ_l, is higher than that for atoms to jump from the left to the right, Γ_r. This means that atoms can flow from the right to the left even when the composition at the left is higher than that at the right. The net flux of atoms then becomes

$$J = \left(C - \frac{1}{2}\frac{\partial C}{\partial x} \cdot a\right) \cdot a \cdot \Gamma_r - \left(C + \frac{1}{2}\frac{\partial C}{\partial x} \cdot a\right) \cdot a \cdot \Gamma_l = (\Gamma_r - \Gamma_l) \cdot a \cdot C - \frac{\Gamma_r + \Gamma_l}{2} \cdot a^2 \cdot \frac{\partial C}{\partial x} \tag{3.4}$$

It can be seen that if $\Gamma_r = \Gamma_l = \Gamma$, Eq. (3.4) reduces to Eq. (3.1).

In our discussion, we assume that the material density N_v (total number of atoms per unit volume) is a constant. For the diffusion species, its composition, C, is related to its atomic fraction X as C = $\mathrm{N}_v \cdot$ X. Because the Gibbs free energy for equilibrium solid solutions is a function of atomic fraction,[54] the local energy (per atom) can be taken as a function of local composition so that we can write E = E(C). E(C) is a material property and can be pre-determined. E(C) and the local composition profile determine the energy change during atom jumps, which in turn determines the atom jump frequency.

Consider a system where a uniform composition is maintained. In this case, atom jumps do not change the energy. As a result, atom jumps are associated with a constant energy barrier. Note that atom jumps will be associated with a different constant energy barrier if the system is maintained at a different uniform composition. This means that the activation energy barrier of jumps in systems with uniform compositions can also be viewed as a function of composition, Q = Q(C). Like E(C), Q(C) can also be pre-determined. Q(C) can be extracted from the average diffusion

distance of atoms as a function of temperature for systems with constant compositions. Using the Arrhenius equation, the jump frequency in a uniform system can be expressed as a function of composition:

$$\Gamma_0(C) = \frac{1}{2} \cdot \nu \cdot \exp\left[-\frac{Q(C)}{k \cdot T}\right] \tag{3.5}$$

where k and T are respectively Boltzmann constant and temperature, ν is vibration frequency, and the factor $\frac{1}{2}$ is introduced to account for the jumps in two directions.

If the composition is not uniform, atoms experience a composition change to their environment during the jumps. Due to the dependence of energy on composition, the energy barrier of the jump becomes a function of the local composition gradient and jump direction. To calculate the energy barrier, the energy change during the jump needs to be determined. The expression for the energy change associated with an atom jump to an adjacent plane needs to be sufficiently precise so that the non-random diffusion processes responsible for phenomena such as a spinodal decomposition can be addressed. It is necessary to note that when an atom jumps from one plane to another, the compositions, and hence, the energies, change at both planes. Referencing Fig. 3.1, we assume that the total number of atoms per plane is N, and the left and the right planes have N_l and N_r jumping atoms, respectively. The corresponding volume compositions at the left and the right planes are then $C_l = N_v \cdot \frac{N_l}{N}$ and $C_r = N_v \cdot \frac{N_r}{N}$. The energy per unit area of the cross section of the material will then become

$$E_t = N \cdot E(C_l) + N \cdot E(C_r) \tag{3.6}$$

If number of atoms per plane is constant (equivalent to constant N_v and constant lattice constant), $dN_l + dN_r = 0$. The derivative of E_t with respect to N_r then gives,

$$\frac{dE_t}{dN_r} = N_v \left[\frac{\partial E(C_r)}{\partial C_r} - \frac{\partial E(C_l)}{\partial C_l}\right] \approx N_v \cdot \frac{\partial^2 E}{\partial C^2} \cdot (C_r - C_l) \tag{3.7}$$

Here unless explicitly specified, the derivatives (e.g., $\frac{\partial^2 E}{\partial C^2}$) are evaluated at the average composition $(C_l+C_r)/2$. From Eq. (3.7), we can write the energy change for an atom to jump from the left to the right plane as,

$$\Delta E = N_v \cdot \frac{\partial^2 E}{\partial C^2} \cdot \frac{\partial C}{\partial x} \cdot a \tag{3.8}$$

It can be seen that Eq. (3.8) incorporates the second derivative of the energy with respect to composition which is the essential driving force for spinodal decompositions. Because the energy barrier equals Q(C) + $\Delta E/2$ for jumps to the right and Q(C) - $\Delta E/2$ for jumps to the left, the two Arrhenius equations are:

$$\Gamma_l = \min\left[\nu, \Gamma_0 \cdot \exp\left(\frac{\Delta E}{2 \cdot k \cdot T}\right)\right] \tag{3.9}$$

and

$$\Gamma_r = \min\left[\nu, \Gamma_0 \cdot \exp\left(-\frac{\Delta E}{2 \cdot k \cdot T}\right)\right] \tag{3.10}$$

Note that we bound Γ_l and Γ_r in Eqs. (3.9) and (3.10) by the vibration frequency ν. This is because the jump frequency cannot exceed the vibration frequency even if the energy barrier becomes zero or negative. Substituting Eqs. (3.9) and (3.10) into Eq. (3.4) gives,

$$\begin{aligned} J &= \left\{\min\left[\frac{\nu}{\Gamma_0}, \exp\left(-\frac{\Delta E}{2 \cdot k \cdot T}\right)\right] - \min\left[\frac{\nu}{\Gamma_0}, \exp\left(\frac{\Delta E}{2 \cdot k \cdot T}\right)\right]\right\} \cdot \Gamma_0 \cdot a \cdot C \\ &- \frac{1}{2}\left\{\min\left[\frac{\nu}{\Gamma_0}, \exp\left(-\frac{\Delta E}{2 \cdot k \cdot T}\right)\right] + \min\left[\frac{\nu}{\Gamma_0}, \exp\left(\frac{\Delta E}{2 \cdot k \cdot T}\right)\right]\right\} \\ &\cdot \Gamma_0 \cdot a^2 \cdot \frac{\partial C}{\partial x} \end{aligned} \tag{3.11}$$

If E(C) and Q(C) are known, Eq. (3.11) provides a complete description of the flux. It can be seen that if energy is independent of composition, $\frac{\partial E}{\partial C} = 0$, Eq. (3.11) correctly reduces to Eq. (3.1). Moreover, substituting Eq. (3.11) into Eq. (3.2) gives a partial differential equation for the non-random diffusion process.

In many practical processes where smoothly varying energy functions and composition profiles are encountered, ΔE can be very small. In this case, Eq. (3.11) can be simplified to first order as

$$J = -\frac{\Delta E}{k \cdot T} \cdot \Gamma_0 \cdot a \cdot C - \Gamma_0 \cdot a^2 \cdot \frac{\partial C}{\partial x} \tag{3.12}$$

It is clear that the first term captures the energy driven diffusion and the second term is the normal composition driven diffusion. Substituting Eq. (3.8) into Eq. (3.12) results in

$$J = -\frac{\Gamma_0 \cdot a^2}{k \cdot T}\left(N_v \cdot C \cdot \frac{\partial^2 E}{\partial C^2} \cdot \frac{\partial C}{\partial x} + k \cdot T \cdot \frac{\partial C}{\partial x}\right) \tag{3.13}$$

Using Eq. (3.2), we obtain a partial differential equation:

$$\frac{\partial C}{\partial t} = \frac{a^2}{k \cdot T}\frac{\partial}{\partial x}\left(\Gamma_0 \cdot N_v \cdot C \cdot \frac{\partial^2 E}{\partial C^2} \cdot \frac{\partial C}{\partial x} + k \cdot T \cdot \Gamma_0 \cdot \frac{\partial C}{\partial x}\right) \tag{3.14}$$

Eq. (3.14) essentially incorporates the same energy driven diffusion term encountered in Cahn-Hilliard equations [48]. It can be seen that if $\frac{\partial E}{\partial C} = \frac{\partial^2 E}{\partial C^2} = \frac{\partial Q}{\partial C} = 0$, Eq. (3.14) correctly reduces to the Eq. (3.3). It should be noted that the equations derived above do not consider the effects of stress. These effects, however, can be incorporated by analogous modifications of Eq. (3.8).

3.3 Diffusional Monte Carlo Simulation Method for Random Diffusion

Conventional kinetic Monte Carlo methods simulate each atom jump based upon the relative jump frequencies of all the atoms. Regardless of atom jump sequences, all atoms reside at lattice locations after completion of the diffusion process. We can assume that the probability density distribution function for an atom i to exist in a small spatial region between $\mathbf{r}_i$ and $\mathbf{r}_i+\mathbf{dr}_i$ from its original site is $\rho(\mathbf{r}_i)$, where i = 1, 2, ..., N, and N is the total number of atoms in the system. During random diffusion, the diffusion of each atom can be considered independent. The probability density for the total diffusion distance of each of the atoms (a function of the annealing time and diffusivity coefficient) can be found from random walk statistics as summarized in Appendix, section 3.6. Once $\rho(\mathbf{r}_i)$ is known, then the diffusion of each atom over the entire diffusion process could be simulated in one step by statistically moving the atom to the corresponding location $\mathbf{r}_i$ in accordance with the relative probability $\rho(\mathbf{r}_i)$. A system containing N atoms then requires N such steps to simulate the diffusion of all atoms and the final atom positions well represent the annealed structure.

Just like the conventional kMC methods, the N-step simulation results in a discrete structure. The atomic composition profiles obtained using such a simulation may be substantially different to that obtained using the continuum theories. It is useful to recall that Metropolis Monte Carlo methods[55] calculate the average properties of a large number atomic configurations (atom positions) that are sampled based upon Boltzmann energy distribution that is representative of equilibrium structures. As a result, Metropolis Monte Carlo methods are able to predict accurate equilibrium properties.[55] The only difference between the kinetically determined structure and the equilibrium one is that the atom positions satisfy a kinetic position distribution $\rho(\mathbf{r}_i)$ instead of the Boltzmann distribution. As a result, the conceptual framework of Metropolis Monte Carlo methods could in principle be used to address kinetics problems. Details are discussed in the following.

A material system configuration can be denoted by an assembly of position vectors, $\{\mathbf{r}_i\}$, to all the N atoms in a system; i = 1, 2, ..., N. Any change of position of any of the atoms then results in a change of the system configuration. If a material is annealed at a temperature T for a period of time t, its configuration continuously changes due to the diffusion of atoms in the system. The diffusion distance of a given atom is not deterministic, but satisfies a known probability density distribution. For random diffusion in one-, two-, and three- dimensions, the diffusion distance probability density functions are given by Eqs. (3.26), (3.28), and (3.30) in Appendix, section 3.6. Each equation relates the diffusion distance to an annealing time, t, and a diffusivity coefficient, D. The diffusivity coefficient depends on absolute temperature, T, through the Arrhenius equation: $D = D_0 \cdot \exp\left(-\frac{Q}{kT}\right)$, where D_0 is pre-exponential diffusion coefficient, Q is activation energy barrier of diffusion, and k is Boltzmann constant. As a result, the effects of both T and t are incorporated in the diffusion

distance probability density functions.

The simulated structures after diffusion in a system containing a limited number of atoms are unlikely to be exactly that experimentally observed. However, if the calculations are repeated many times, the averaged experimental observations and predictions should converge. This means that any measurable property of the system, such as the composition profile, can be accurately calculated as the average property of all the possible configurations of the system. Here the property, p, of a given system configuration can be viewed as a unique function of the atom positions $\{\mathbf{r}_i\}$ so that it is possible to write $\mathrm{p} = \mathrm{p}(\{\mathbf{r}_i\})$.

Given that the probability density for an atom i to exist in a small spatial region between $\mathbf{r}_i$ and $\mathbf{r}_i+\mathbf{dr}_i$ is $\rho(\mathbf{r}_i)$, and if this probability density is independent of the positions of the other atoms, then the probability density for the system to have atoms occupying sites between $\{\mathbf{r}_i\}$ and $\{\mathbf{r}_i+\mathbf{dr}_i\}$ (i = 1, 2, ..., N) is $\rho(\mathbf{r}_1)\rho(\mathbf{r}_1)...\rho(\mathbf{r}_N)$. The average property of the system can then be defined as weighted sum of the properties of all possible configurations:

$$\bar{p} = \int_{-\infty}^{\infty}\int_{-\infty}^{\infty}\cdots\int_{-\infty}^{\infty} p\left(\{\mathbf{r}_i\}\right)\rho\left(\mathbf{r}_1\right)\rho\left(\mathbf{r}_2\right)\ldots\rho\left(\mathbf{r}_N\right)d\mathbf{r}_1 d\mathbf{r}_2\ldots d\mathbf{r}_N \tag{3.15}$$

However, since a material system includes a very large number of atoms, the direct use of Eq. (3.15) to calculate the property of a system is not a computationally practical approach to material property prediction.

Suppose a large number, N_s, of system configurations are sampled in such a way that positions of each atom i (i = 1, 2, ..., N) collected from these configurations statistically satisfy the corresponding distribution, $\rho(\mathbf{r}_i)$. The average property of the system is then simply approximated as the average property of these sampled configurations:

$$\bar{p} = \frac{1}{N_s}\sum_{m=1}^{N_s} p_m \tag{3.16}$$

where p_m is the property of the m-th sampled configuration. From these definitions, it is obvious that Eqs. (3.15) and (3.16) give exactly the same average property when $\mathrm{N}_s \to \infty$.

In the dMC simulation approach suggested here, an initial material configuration is created as an assembly of atoms whose coordinates are assigned according to a desired initial structure (prior to annealing). This configuration can be sampled as the first configuration. The property of interest is calculated for this configuration and recorded.

The second configuration is sampled as a variation of the first configuration by allowing a randomly selected atom to diffuse. Unlike the kMC method that simulates individual atomic jumps, each dMC step simulates the total diffusion of one atom over the entire annealing period using the random walk probability distribution, ρ(r), given in Eqs. (3.26), (3.28), and (3.30). To statistically choose the total

diffusion distance r such that it satisfies a normalized probability density function ρ(r) $\left(i.e., \int_0^\infty \rho\left(r\right) dr = 1\right)$, a random number R between zero and one is first created and r is then deduced from solution of the equation $\int_0^r \rho\left(r\right) dr = R$. An explicit expression relating r to R can be derived for the two-dimensional case as r = $2\sqrt{-Dt \cdot \ln\left(1-R\right)}$. No simple explicit expressions of r have been found for the one- and three-dimensional cases but they can be numerically pre-computed. To avoid solving for r during each dMC step, r can then be explicitly expressed as a cubic spline function of R for the one- and three-dimensional cases where the cubic spline function parameters are pre-tabulated by fitting to the numerical calculations.

Once r is known in terms of R, t, and T (via D), the selected atom is displaced by the distance, r, in a selected direction. For one-dimensional simulations, the atom is moved in either direction with an equal probability. For two- and three-dimensional simulations, the direction of the displacement is randomly chosen. Once the selected atom is displaced, the property of the resulting configuration is calculated and is included in the calculation of a running average of the data recorded for previous configurations (in this case, the first configuration).

The third configuration is sampled by a variation of the second configuration. In this dMC step, a new randomly selected atom is displaced with respect to its initial position (i.e., the coordinates in the first configuration) according to the random walk diffusion statistics. The property of the third configuration is calculated and is included in the calculation of the running average along with data recorded for all previous configurations. The fourth configuration is sampled similarly, and so on, until a sufficiently large number, N_s, of configurations are sampled to result in a well converged average property of the system.

It should be pointed out that as the dMC steps continue, the diffusion is simulated for more and more atoms, and the currently sampled configuration may be quite close to the true post-annealed structure. Even so, a single configuration is always less accurate than the averaged configuration for representation of the post-annealing structure. In addition, since the data is averaged over a very large number of configurations, the result becomes insensitive to the choice of the first configuration even though it is taken as the initial configuration (prior to annealing) and therefore might deviate significantly from the post-annealing structure. Alternatively, a designated number of the earliest sampled configurations could be excluded from the average property calculations to improve the convergence. It can now be seen that a difference between kMC and dMC methods is that a single kMC simulation represents a single measurement of the material structure while the result of a single dMC simulation is the averaged outcome of a large number of dMC steps, each measuring a sampled configuration. As a result, dMC simulations of diffusion can be viewed as averaged simulations of many kMC runs and are anticipated to produce results much closer to those obtained from Fick′s laws of diffusion than is usually possible with kMC simulations.

The dMC method is not diffusion time limited. As a result, it can be used to address

diffusion over time scales that are unlikely to be achievable with conventional kMC methods. For example, the dMC method can be used to simulate a kinetic process that persists for 10^{10} years. While the dMC method appears to be more computationally efficient than the kMC method in this case, it only calculates the final structure at the (targeted) simulated time, while a kMC simulation yields many intermediate structures at various times up to the (targeted) simulated time.

3.4 Results

In this section, we investigate the validity and precision of the dMC method. An activation energy barrier for jumping, Q = 1.161 eV, and a pre-exponential factor, D_0 = 3.607×10^{-6} Å^2/ps, are used. These diffusion parameters are in the range of experimental inter-diffusion coefficients for the Cu-Ni, Cu-Pd, and Cu-Pd-Fe systems.[56] However, they do not refer to any particular materials and are used here only to explore the approach. Selected examples of one-, two-, and three-dimensional diffusion at a temperature of 600 K are first solved, and the results are compared with those obtained from Fick′s equation for random diffusion. The calculations are carried out to examine the time evolution of the solute composition profiles in a solute-solvent material system. The method is then applied to simulate the evolution of a spinodal structure composed of polystyrene (PS), poly(2-chlorostyrene) (P2CLS), and di-n-butyl phthalate (DBP) during annealing at a single-phase temperature, and the results is compared with the corresponding experiments.[57] Since volume composition scales with atomic fraction under our assumption, we present our work using atomic fraction for convenience.

3.4.1 One-Dimensional Diffusion

The one-dimensional Fick′s equation of diffusion for an infinitely long rod placed on the x- axis is described by Eq. (3.3). For problems with simple initial and boundary conditions, Eq. (3.3) can be analytically solved. Two such simple examples were chosen for study. The first explored the central diffusion problem where a solute-rich region was placed in the middle of an infinitely long solvent rod. The initial composition (referred here as atomic fraction) profile was represented by $X(x, t = 0) = X_0 \cdot \exp\left(-\frac{x^2}{4Dt_0}\right)$, where X_0 is the peak solute composition at x = 0 and t_0 is a parameter with the unit of time. Here we assume X_0 = 100% and t_0 = 1.006×10^8 ps. In this composition profile, the high solute composition at x = 0 quickly decays to near zero at x = ± 80 Å. Using this initial composition profile, Eq. (3.3) can be analytically solved to yield:

$$X(x,t) = X_0\sqrt{\frac{t_0}{t}} \cdot \exp\left[-\frac{x^2}{4D(t_0+t)}\right] \tag{3.17}$$

The second example explored periodic diffusion along an infinitely long rod. The initial composition profile was represented by a periodic function: $X(x, t=0) = X_0 + \frac{\Delta X}{2} \cdot \cos\left(\frac{2\pi}{L_x} x\right)$, where X_0 is the average composition along the rod, ΔX is the amplitude of the composition variation, and L_x is the periodic length in the rod direction. Here we use $X_0 = 58.8\%$, $\Delta X = 80\%$, and $L_x = 400$ Å. With this initial condition, Eq. (3.3) can also be analytically solved to give:

$$X(x,t) = X_0 + \frac{\Delta X}{2} \cdot \exp\left[-\left(\frac{2\pi}{L_x}\right)^2 Dt\right] \cdot \cos\left(\frac{2\pi}{L_x} x\right) \tag{3.18}$$

To carry out the corresponding dMC simulations, a one-dimensional computational rod with a total length of 400 Å was used (in conjunction with the periodic boundary condition). This rod was divided into 50 grids with each grid measuring 8 Å. Each grid was assigned 40 atoms of either solute or solvent. The relative numbers of the two types of atoms were chosen to best match the initial composition profile. Atoms in the grid were assumed to take the same position as the grid coordinates. This simulated system contained a total of 2000 atoms. Note that the number of atoms assigned to the grid affects the resolution of the calculated atomic fraction. It does not have any implications on material density.

The dMC method described above was then used to calculate the average composition of all sampled configurations. The number of configurations required to produce the highly converged results depends on the simulated conditions and system size. During annealing, the initial composition profile continuously approached the final composition profile. The composition uniformity that is characteristic of a composition profile can be quantified by mean square deviation of the composition profile from the average composition. This composition uniformity parameter was used to measure the converging status of the simulations. An example of a convergence test with a simulated central diffusion that lasted for 1.006×10^8 ps is shown in Fig. 3.2. It plots the running average of the mean square deviation of the composition profile as a function of the number of the dMC steps. It can be seen that the simulated result is well converged when the number of sampled configurations exceeds 2×10^5. We also found that for the central diffusion conditions simulated, a dMC step number of 10^7 generally produced good results for all the annealing times simulated. For the periodic diffusion case, we found that $\sim 10^9$ dMC steps were required to yield converged calculations for numerous simulations using different annealing times. In general, larger systems and longer diffusion distances require more dMC steps to achieve well converged results.[1] It should be noted that a discrete annealed structure can always be calculated using the N-step simulation described above. The N-step simulation is not expected to produce results that precisely match those obtained from continuum simulations. Its computational cost, however, always equals the N dMC steps.

With the parameters selected and convergence conditions determined, the annealing

[1] In our simulations, we found that 10^{10} dMC steps took 4-5 days on a single processor of a Birch Linux Cluster.

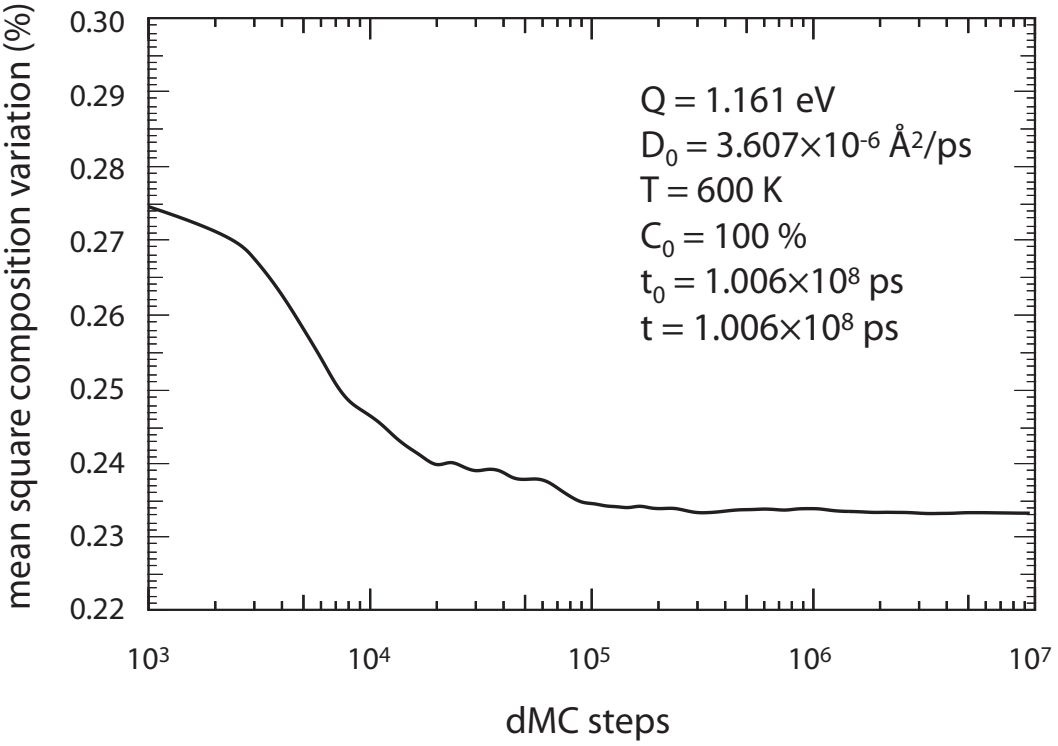

Figure 3.2. The convergence test for the one-dimensional central diffusion simulation using a diffusion time of 1.006×10^8 ps. The running average of the mean square variation of the composition profile is shown as a function of the number of the dMC steps.

of the rods with both central and periodic initial composition profiles were simulated for different annealing times at the fixed annealing temperature of 600 K. The results are compared with the exact (Fick′s laws) solutions in Fig. 3.3(a) for the central diffusion case and in Fig. 3.3(b) for the periodic diffusion case. Fig. 3.3(a) shows that during the central diffusion simulations, the initial sharp peak of the composition at x = 0 continuously decays and the width of the composition profile became continuously broader. The detailed composition profiles predicted from the dMC simulations for different annealing times between 0 and 4.022×10^8 ps are virtually indistinguishable from the exact solutions. It should be noted that at an annealing time of 4.022×10^8 ps, the composition profile spreads to the entire simulated length scale of 400 Å. Due to the periodic boundary condition used in the dMC simulations, a further increase in the simulated annealing time would cause an interaction between adjacent (periodic) images of the composition peaks. As a result, the simulated results for annealing times beyond 4.022×10^8 ps could not be compared with the analytical solution that corresponds to a truly isolated composition peak. The periodic diffusion problem does not suffer from this problem and allows the results of the dMC simulations to be compared with the analytical solution for any annealing time. Fig. 3.3(b) shows that during periodic diffusion, the amplitude of the composition oscillation continuously decreased as the annealing time was increased to 2.848×10^{19} ps. At 2.848×10^{19} ps, the composition became essentially uniform in the scale used in the figure. This uniform composition had converged to the initial average composition, $C_0 = 58.8\%$. During the entire time evolution from the initial composition profile to the final uniform composition profile, the results obtained from the dMC simulations are virtually indistinguishable from the exact analytical solution. The dMC method clearly provides highly precise estimates of one-dimensional random diffusion processes.

3.4.2 Two-Dimensional Diffusion

Diffusion from a central source in an infinitely large plate can be described by a radially symmetric, two-dimensional Fick′s equation of diffusion:

$$\frac{\partial C}{\partial t} = D \cdot \left(\frac{\partial^2 C}{\partial r^2} + \frac{1}{r} \frac{\partial C}{\partial r} \right) \tag{3.19}$$

For a simple case of central diffusion where a circular cylinder of solute-rich material is placed in the middle of a large solvent plate, the initial composition profile can be described by: $X\left(r, t=0\right) = X_0 \cdot \exp\left(-\frac{r^2}{4Dt_0}\right)$. Here it is assumed that $X_0 = 97.5\%$ and $t_0 = 1.006\times10^8$ ps. In this case, the high solute composition at r = 0 quickly decays to near zero at r = 80 Å. With this simple initial condition, Eq. (3.19) has an analytical solution:

$$X\left(r,t\right) = X_0 \cdot \frac{t_0}{t} \cdot \exp\left[-\frac{r^2}{4D\left(t+t_0\right)}\right] \tag{3.20}$$

The two-dimensional dMC simulations used a 400×400 Å^2 square-shaped computational material with periodic boundary conditions in the two orthogonal (x, y)

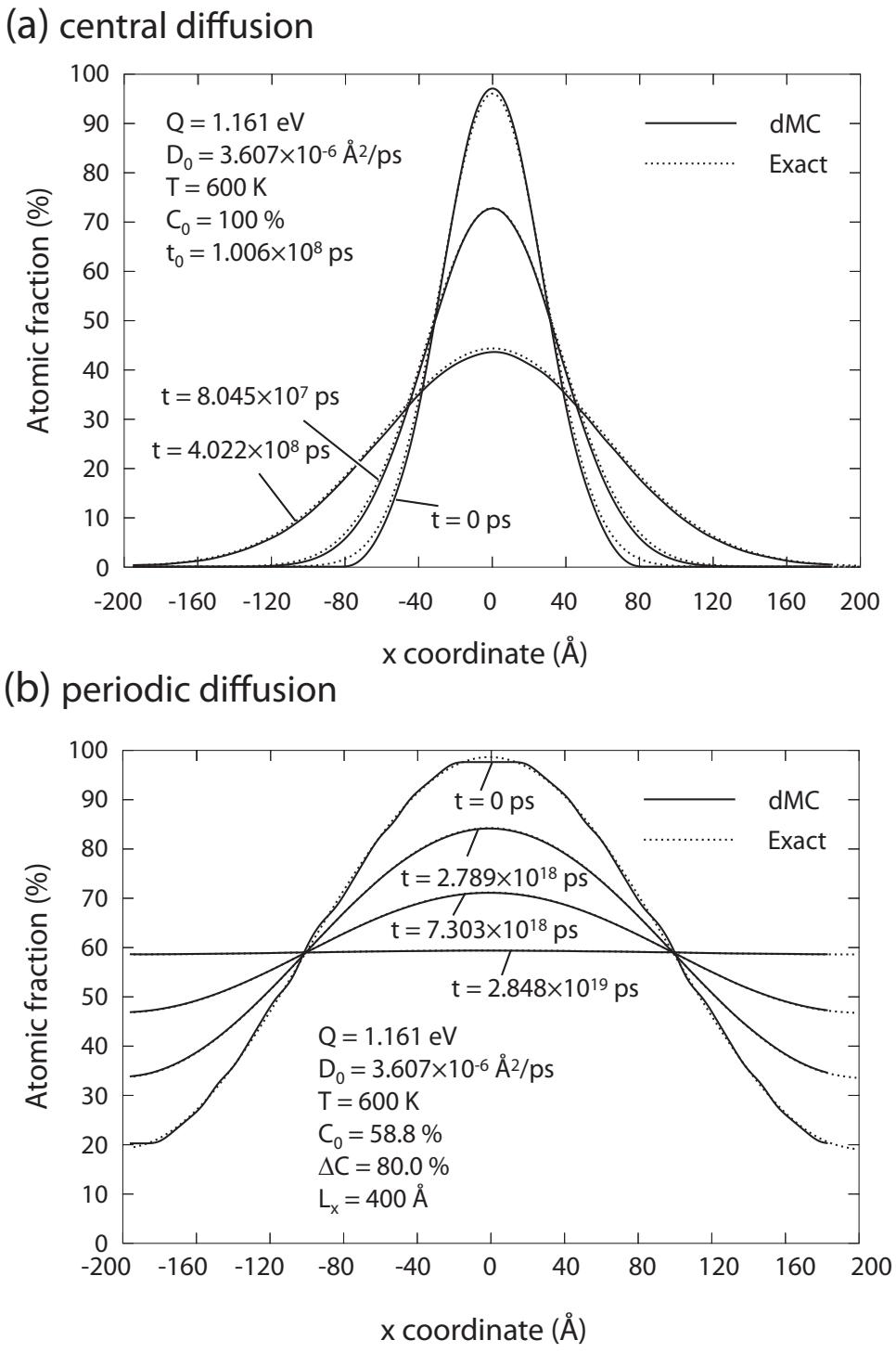

Figure 3.3. Time evolution of composition profiles during one-dimensional diffusion. (a) central diffusion; and (b) periodic diffusion.

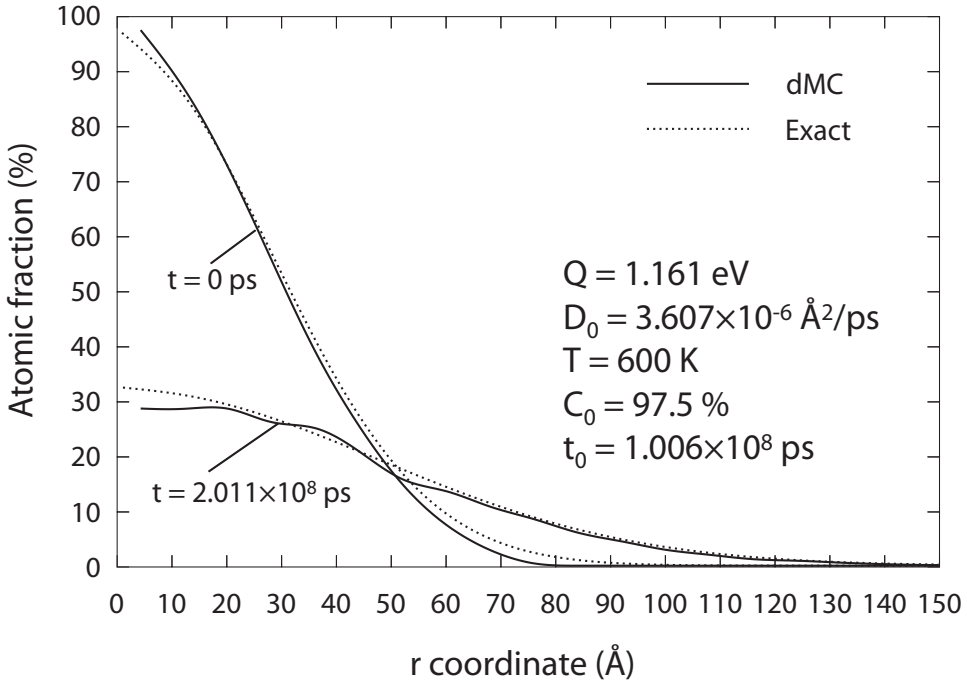

Figure 3.4. Time evolution of composition profiles during two-dimensional central diffusion.

directions of the plane. The plate was divided into 50×50 grids, each measuring 8×8 Å^2. Each grid was assigned 40 atoms of either solute or solvent according to the initial composition profile. This system therefore contained a total of 100,000 atoms.

A total of 10^{10} dMC steps were used to calculate the converged average composition profiles. Due to the symmetry of the problem, the composition profile was represented as a function of the radial distance, r = $\sqrt{x^2+y^2}$, from the central point. The composition profiles obtained from the dMC simulations for two annealing times of 0 and 2.011×10^8 ps are compared with the corresponding curves calculated using Eq. (3.20) in Fig. 3.4. It shows that the annealing for 2.0×10^8 ps significantly broadened the initial sharp distribution of the composition. Fig. 3.4 also shows that the difference between dMC results and the exact solution becomes relatively more significant when the r coordinate decreases. This is likely to be caused by statistics because the material volume used to average the composition is reduced when r decreases. Nonetheless, the general composition profile obtained from the dMC simulation is seen to be very similar to the exact solution, and it would appear that the dMC method effectively captures the two-dimensional diffusion processes.

3.4.3 Three-Dimensional Diffusion

Central diffusion from a spherical source in an infinitely large bulk sample is the simplest three-dimensional case to investigate. The diffusion in such a problem can be described by a radially symmetric three-dimensional form of Fick′s equation of diffusion:

$$\frac{\partial C}{\partial t} = D\left(\frac{\partial^2 C}{\partial r^2} + \frac{2}{r}\frac{\partial C}{\partial r}\right) \tag{3.21}$$

The initial central diffusion source is defined by an initial composition profile $X\left(r, t=0\right) = X_0 \cdot \exp\left(-\frac{r^2}{4Dt_0}\right)$. Here it is assumed that $X_0 = 92.5\%$ and $t_0 = 6.436\times10^7$ ps. In this composition profile, the central peak composition decays to near zero at r = 70 Å. Given this initial condition, Eq. (3.21) has an analytical solution:

$$X\left(r,t\right) = X_0 \cdot \frac{t_0}{t} \cdot \sqrt{\frac{t_0}{t}} \cdot \exp\left[-\frac{r^2}{4D\left(t+t_0\right)}\right] \tag{3.22}$$

A three-dimensional computational bulk material with a 320×320×320 Å^3 dimension and periodic boundary conditions (in x, y, and z directions) was used for the three-dimensional dMC simulations. The computational volume was divided into 40×40×40 grids with each grid measuring 8×8×8 Å^3. Each grid contained 40 solute or solvent atoms that are assigned according to the initial composition profile. The entire simulated system contained 2,560,000 atoms.

A total of 10^{10} dMC steps were used to calculate the converged average composition profiles at two simulated annealing times of 0 and 6.436×10^7 ps. The resulting curves of composition as a function of the radial distance, r = $\sqrt{x^2+y^2+z^2}$, from the central diffusion source are compared with those calculated using Eq. (3.22) in Fig. 3.5. It can be seen that the 6.436×10^7 ps annealing significantly broadened the composition distribution. For the same reason as described above, the difference between dMC results and the exact solution becomes relatively more significant when the r coordinate decreases. However, the general annealing time dependent composition vs. radius profiles obtained from the dMC method are again virtually indistinguishable from those solved from the Fick′s equation. The dMC method can hence be accurately used to simulate the three-dimensional diffusion processes.

3.4.4 Dissolution of Spinodal Structure

Okada, Tao, and Nose have used electron microscopy to study the microstructure evolution of a PS/P2CLS/DBP spinodal polymer during annealing at a temperature in a single phase domain.[57] An example pre-annealed structure is shown in Fig. 3.6(a). Their two dimensional electron micrographs of the structure before annealing were divided into 356×258 grids, with each grid measuring 188×188 Å^2. A model composition for each of the grids was then assigned based on the corresponding gray

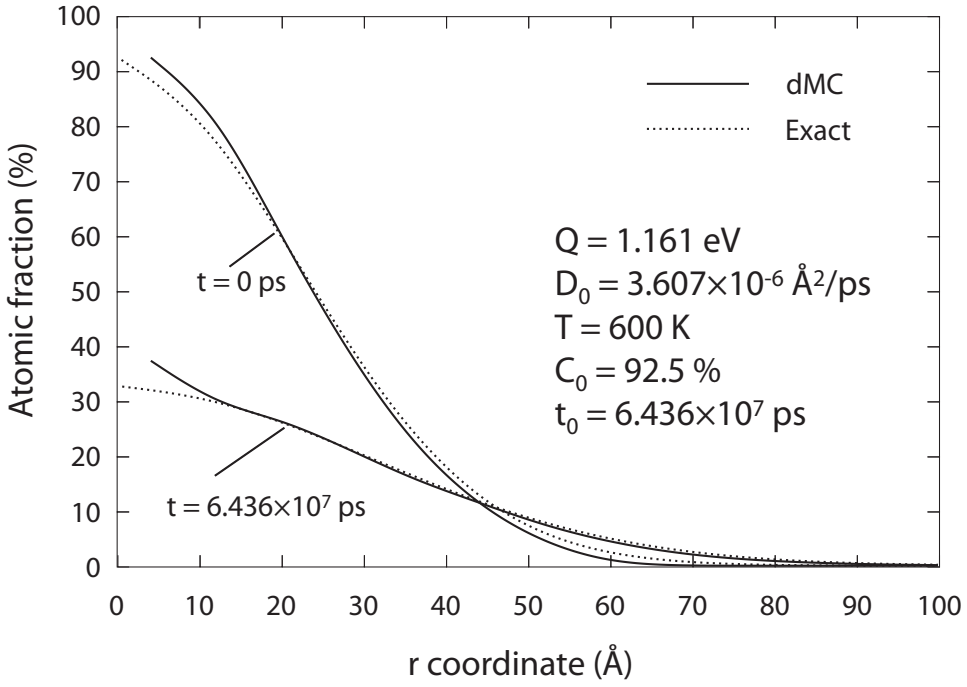

Figure 3.5. Time evolution of composition profiles during three-dimensional central diffusion.

scale level in the experimental images. The two-dimensional dMC method was then used to anneal the digitized structure. Electron micrographs of the experimental structure before and after annealing, as well as the simulated structure after annealing, are shown in Figs. 3.6(a)-(c) respectively. Note that while Fig. 3.6(c) corresponds to the same area as Fig. 3.6(a), Fig. 3.6(b) is likely to correspond to a different area. It can be seen that the simulation well captures the structure evolution during real experiments.

3.4.5 Spinodal Decomposition

In section 3.2, we developed an atomistic theory of non-random diffusion that resulted in analytical equations, Eqs. (3.11) - (3.14). In principle, the dMC method described above can be applied to these non-random diffusion problems. However, since the diffusion behavior of each atom depends on the varying composition profile, the simulation of a slow process needs to be divided into small time intervals so that the atom behavior within each of the short time slots can be approximately treated as quasi-constant. This is also computationally acceptable if the N-step simulation method is used (rather than sampling a large number of configurations). In that case, a computational cost of 10^{10} dMC steps would allow total time to be divided into 10^4 intervals for a system containing 10^6 atoms. The fine resolution of time in-

(a) initial spinodal structure, electron micrograph

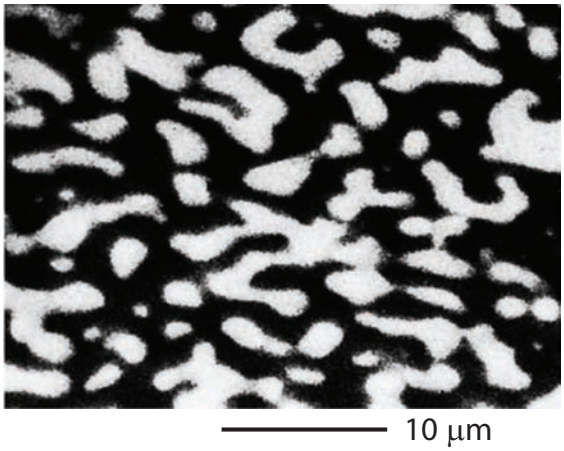

(b) after annealing, electron micrograph

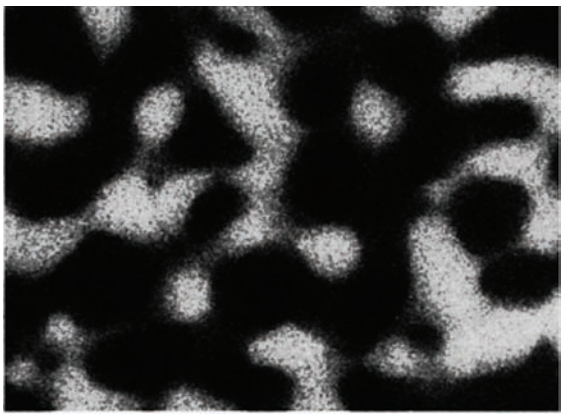

(c) after annealing, dMC simulation

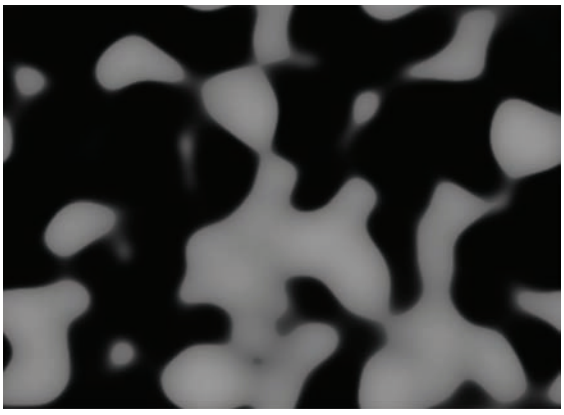

Figure 3.6. Evolution of PS/P2CLS/DBP spinodal structure during annealing at a temperature in a single-phase domain. (a) electron micrograph of an initial spinodal structure; (b) electron micrograph of an annealed spinodal structure; and (c) the dMC predicted micrograph of the annealed spinodal structure.

tervals should then ensure the accuracy of the approach. Such a dMC method will be explored in the future. Here we validate the theory by using MATHEMATICA′s NDSolve function to directly solve Eq. (3.14) for a spinodal decomposition process during annealing at 900 K. We assume that composition satisfies $0 \leq C \leq C_{max}$, where the maximum composition C_{max} refers to the one when all solute sites are occupied.

For a solid solution to exhibit the spinodal decomposition behavior, its Gibbs energy as a function of composition must have two minima. For simplicity, we assume that $E(X) = 0.5 \cos(4\pi \cdot X)$. The Gibbs free energy, which is expressed as $G(X) = E(X) + k \cdot T \cdot [X \cdot ln(X) + (1 - X) \cdot ln(1 - X)]$, has two minimums as shown in Fig. 3.7(c). The diffusion energy barrier is assumed to be independent of composition and the same diffusion parameters as above are used. Two initial compositions of the solid solution prior to the spinodal decomposition are considered. The first assumes that the composition is near-uniform but with seven small oscillations to initiate the decomposition. The second has a single large initial composition oscillation to enable more detailed examination of the decomposition. These initial composition profiles are shown using dashed lines in Figs. 3.7(a) and 3.7(b). Eq. (3.14) is then solved for the structure evolution under the boundary condition that the flux at the left bound (x = -200 Å) equals the flux at the right bound (x = 200 Å). The composition profiles obtained after annealing at 900 K for 1 and 10 sec. respectively for the two initial compositions are shown using solid lines in Figs. 3.7(a) and 3.7(b).

Fig. 3.7(a) indicates that after annealing at 900 K for 1 sec., the initial near-uniform composition profile develops amplified oscillations. The difference between the minimum and the maximum composition in Fig. 3.7(a), however, is smaller than equilibrium composition gap shown in Fig. 3.7(c). This is expected because diffusion is driven by both the composition gradient and the energy differential. When the period between spinodal oscillations is small, the composition gradient becomes large. Because the composition gradient always promotes uniform composition distribution, it reduces the composition oscillation amplitude from the equilibrium composition miscibility gap. Fig. 3.7(b) indicates that after annealing at 900 K for ten sec., the initial big composition oscillation is even further separated. Because only one composition oscillation is examined, the composition gradient is much less significant. It can be seen that at the reduced composition gradient, the equilibrium compositions of the two separated phases are indeed pushed towards the minimum energy compositions of 25 % and 75 % shown in Fig. 3.7(c). As a result, Fig. 3.7 indicates that Eq. (3.14) captures the physics needed for modeling the non-random diffusion processes such as spinodal decomposition.

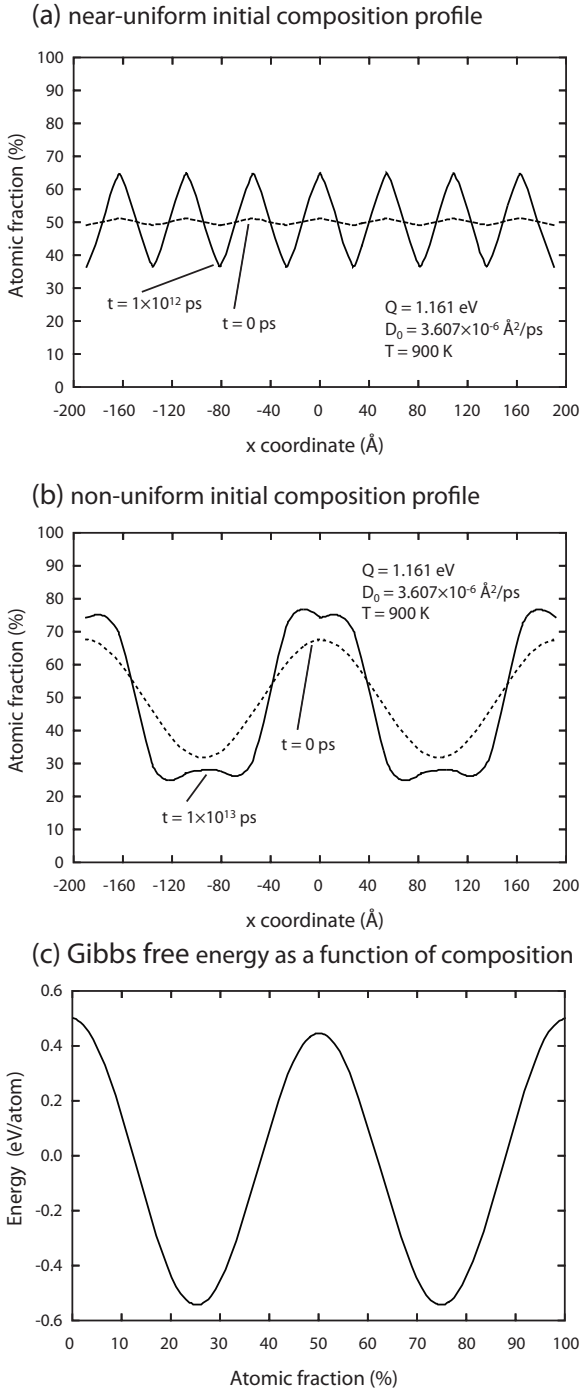

Figure 3.7. Spinodal decomposition. (a) near-uniform initial composition profile; (b) non-uniform initial composition profile; and (c) Gibbs free energy as a function of composition.

3.5 Conclusions

The atomistic diffusion theory of mass transport has been developed and used to construct partial differential equations for both random and non-random diffusion. A diffusional Monte Carlo method for simulating the kinetics of material evolution has been proposed for random diffusion. Unlike the jump-based kinetic Monte Carlo method, the diffusional Monte Carlo method is based on estimates of the total diffusion distance during the entire simulated time. As a result, the simulation is relatively efficient, especially when the jump frequency becomes extremely high. Because the method calculates the ensemble average property of a large number of configurations, it also produces more reliable results than the kinetic Monte Carlo method. Applications of the method to diffusion problems in one-, two-, and three-dimensions indicate that the diffusional Monte Carlo method can produce almost the same results as those obtained from direct solutions of Fick′s equations of diffusion. It has been successfully used to simulate the dissolution of a spinodal structure during annealing at a temperature in a single-phase domain. The extension of the approach to non-random diffusion is discussed and the application of the non-random diffusion theory during spinodal decompositions is also demonstrated.

3.6 Appendix: Radom Walk Theory

If an atom randomly jumps in a one-dimensional space, then the probability density ρ(r,n) for the atom to fall at a distance r from its starting position after a large number of jumps, n, can be described by a Gaussian probability density distribution function:[58]

$$\rho\left(r,n\right)=\sqrt{\frac{2}{\pi\cdot\sigma\left(n\right)^{2}}}\cdot\exp\left[-\frac{r^{2}}{2\sigma\left(n\right)^{2}}\right] \tag{3.23}$$

where σ(n) is the root-mean-square deviation of r from the mean of the Gaussian distribution ($\bar{r}=0$). σ(n) is a function of the jump number, n, and can be simply expressed as

$$\sigma\left(n\right)^{2}=n\times l^{2} \tag{3.24}$$

Here l is the jump length. The total number of jumps, n, can be calculated from the jump frequency Γ and jump time t as $n=\Gamma\cdot t$. For diffusion problems, T and l can be related to the diffusivity coefficient D. As a result, the random walk distance distribution, Eq. (3.23), can be expressed in terms of D and t rather than n. Here we show that the D and t dependent distance probability density distribution functions can be easily derived from Fick′s equation of diffusion for a particle randomly walking in one-, two-, and three- dimensions.

Consider a single atom at the origin point (x = 0) in a one dimensional x- axis. The initial mass density of the species at x = 0 can then be defined as the average density

over a small section $\left[-\frac{dx}{2}, \frac{dx}{2}\right]$ as C(x = 0, t = 0) = $\frac{1}{dx}$. The initial mass densities of the species at other positions are all zero C(x ≠ 0, t = 0) = 0. C(x, 0) satisfies $\int_{-\infty}^{\infty}$ C(x,0)·dx = 1, and hence can also be viewed as the position probability density distribution of the atom at t = 0. It is recognized that the random walk of a single atom is equivalent to the random diffusion of that atom. As a result, a continuous function of the mass density of the atom after it randomly walks for a period of time t (with a diffusivity coefficient D) can be solved from Eq. (3.3) using the initial condition described above and the mass conservation condition $\int_{-\infty}^{\infty}$ C(x,t,D)·dx = 1:

$$C\left(x,t,D\right)=\frac{1}{2\sqrt{\pi Dt}}\cdot\exp\left(-\frac{x^2}{4Dt}\right) \tag{3.25}$$

It should be pointed out that the mass density distribution of a single atom after one random walk experiment is discrete. The continuous function C(x, t) then cannot represent the discrete mass density distribution of a single random walk experiment. Imagine, however, many such random walk experiments are carried out. The atom is likely to reside at a different location in each experiment. All these locations can then be combined to formulate a continuous position probability density distribution function that can be precisely captured by C(x, t, D). To more clearly see this, we recognize that the coordinates −x and x have the same distance r = $|x|$ from the origin point. The composition profile, Eq. (3.25), can then be directly rewritten as

$$\rho\left(r,t,D\right)=\frac{1}{\sqrt{\pi Dt}}\cdot\exp\left(-\frac{r^2}{4Dt}\right) \tag{3.26}$$

where ρ(r, t, D) represents the probability density for the atom to migrate a distance r away from its initial position after it jumps for a period of time t with a diffusivity coefficient of D. For one-dimensional diffusion, σ^2 = 2Dt. It can be seen that Eq. (3.26) is exactly the same as Eq. (3.23).

Using a similar approach, the two-dimensional random walk distance probability density distribution was derived from Eq. (3.19). First, the solution of Eq. (3.19) yields a mass density distribution function:

$$C\left(r,t,D\right)=\frac{1}{4\pi Dt}\cdot\exp\left(-\frac{r^2}{4Dt}\right) \tag{3.27}$$

Since all positions along the 2πr circular periphery have the same distance from the origin point, the distance probability density distribution can be modified from the mass density distribution function as

$$\rho\left(r,t,D\right)=\frac{r}{2Dt}\cdot\exp\left(-\frac{r^2}{4Dt}\right) \tag{3.28}$$

The three-dimensional random walk distance probability density distribution was derived from Eq. (3.21). The mass density distribution function is:

$$C\left(r,t,D\right)=\frac{1}{4\pi Dt\sqrt{4\pi Dt}}\cdot\exp\left(-\frac{r^2}{4Dt}\right) \tag{3.29}$$

Since all positions over the $4\pi r^2$ spherical surface have the same distance from the origin point, the distance probability density distribution can be written as

$$\rho\left(r,t,D\right)=\frac{r^2}{Dt\sqrt{4\pi Dt}}\cdot\exp\left(-\frac{r^2}{4Dt}\right) \tag{3.30}$$

Eqs. (3.26), (3.28), and (3.30) respectively represent the atom distance distributions after its one-, two-, and three-dimensional random walk diffusion. These distributions can be characterized by a characteristic diffusion distance $d = 2\sqrt{Dt}$. A small characteristic diffusion distance results in a sharp distance distribution over a small diffusion distance range. A larger characteristic diffusion distance is obtained at higher temperatures (which increase D) and longer times. As a result, the diffusion distance distribution becomes more diffused towards a larger distance range.

This page intentionally left blank.

References

[1] Y. Wang, M. Chen, F. Zhou, and E. Ma. high tensile ductility in a nanostructured metal. Nature, 419:912–915, 2002.

[2] A. Romeo, M. Terheggen, D. Abou-Ras, D. L. Bätzner, F. J. Haug, M. Kälin, D. Rudmann, and A. N. Tiwari. development of thin-film cu(in,ga)se_2 and cdte solar cells. Progress in Photovoltaics: Research and Applications, 12:93–111, 2004.

[3] M. N. Baibich, J. M. Broto, A. Fert, F. N. Vandau, F. Fetroff, P. Eitenne, G. Creuzet, A. Friederich, and J. Chazelas. giant magnetoresistance of $(001)fe/(001)cr$ magnetic superlattices. Physical Review Letters, 61(21):2472–2475, 1988.

[4] G. Binasch, P. Grunberg, F. Saurenbach, and W. Zinn. enhanced magnetoresistance in layered magnetic-structures with antiferromagnetic interlayer exchange. Physical Review B, 39(7):4828–4830, 1989.

[5] S. S. P. Parkin. dramatic enhancement of interlayer exchange coupling and giant magnetoresistance in $ni_{81}fe_{19}/cu$ multilayers by addition of thin co interface layers. Applied Physics Letters, 61(11):1358–1360, 1992.

[6] M. Julliere. tunneling between ferromagnetic-films. Physics Letters A, 54(3):225–226, 1975.

[7] B. S. Beech, J. Anderson, J. Daughton, B. A. Everitt, and D. X. Wang. spin dependent tunneling devices fabricated using photolithography. IEEE Transactions on Magnetics, 32(5):4713–4715, 1996.

[8] J. S. Moodera, L. R. Kinder, T. M. Wong, and R. Meservey. large magnetoresistance at room-temperature in ferromagnetic thin-film tunnel-junctions. Physics Review Letters, 74(16):3273–3276, 1995.

[9] F. Eriksson, N. Ghafoor, F. Schafers, E. M. Gullikson, and J. Birch. interface engineering of short-period ni/v multilayer x-ray mirrors. Thin Solid Films, 500(1-2):84–95, 2006.

[10] S. M. Rossnagel. thin film deposition with physical vapor deposition and related technologies. Journal of Vacuum Science and Technology A, 21(5):S74–S87, 2003.

[11] S. M. Rossnagel. directional and ionized physical vapor deposition for microelectronics applications. Journal of Vacuum Science and Technology B, 16(5):2585–2608, 1998.

[12] H. Ono, T. Nakano, and T. Ohta. effects of transition-metals for $cu/m/si$ multilayers (m = cr, ti, nb, mo, ta, w). Applied Physics Letters, 64(12):1511–1513, 1994.

[13] K. W. Kwon, H. J. Lee, and R. Sinclair. solid-state amorphization at tetragonal-ta/cu interfaces. Applied Physics Letters, 75(5):935–937, 1999.

[14] F. Zeng, M. Ding, B. Zhao, and F. Pan. amorphous alloy films formed in an immiscible cu-ta system by ion beam assisted deposition. Materials Letters, 53:40–43, 2002.

[15] B. X. Liu and O. Jin. formation and theoretical modeling of non-equilibrium alloy phases by ion mixing. Physica Status Solidi A, 161:3–33, 1997.

[16] A. L. Greer. metallic glasses. Science, 267:1947–1953, 1995.

[17] T. Masumoto and R. Maddin. structural stability and mechanical properties of amorphous metals. Materials Science and Engineering, 19:1–24, 1975.

[18] J. H. Kim, E. Akiyama, H. Yoshioka, H. Habazaki, A. Kawashima, K. Asami, and K. Hashimoto. the corrosion behavior of sputter-deposited amorphous titanium chromium-alloys in 1-m and 6-m hcl solutions. Corrosion Science, 34(6):975–987, 1993.

[19] H. R. Gong and B. X. Liu. influence of interfacial texture on solid-state amorphization and associated asymmetric growth in immiscible cu-ta multilayers. Physical Review B, 70:134202.1–9, 2004.

[20] H. R. Gong and B. X. Liu. interface stability and solid-state amorphization in an immiscible cu-ta system. Applied Physics Letters, 83(22):4515–4517, 2003.

[21] T. P. C. Klaver and B. J. Thijsse. molecular dynamics simulations of cu/ta and ta/cu thin film growth. Journal of Computer-Aided Materials Design, 10:61–74, 2003.

[22] M. S. Daw and M. I. Baskes. Embedded atom method - derivation and application to impurities, surfaces, and other defects in metals. Physical Review B, 29(12):6443–6453, 1984.

[23] X. W. Zhou, H. N. G. Wadley, R. A. Johnson, D. J. Larson, N. Tabat, A. Cerezo, A. K. Petford-Long, G. D. W. Smith, P. H. Clifton, R. L. Martens, and T. F. Kelly. atomic scale structure of sputtered metal multilayers. Acta Materialia, 49(19):4005–4015, 2001.

[24] X. W. Zhou, R. A. Johnson, and H. N. G. Wadley. misfit energy increasing dislocations in vapor deposited $cofe/nife$ multilayers. Physical Review B, 69(14):144113.1–10, 2004.

[25] W. Zou, H. N. G. Wadley, X. W. Zhou, R. A. Johnson, and D. Brownell. surfactant mediated growth of giant magnetoresistance multilayers. Physical Review B, 64(17):174418.1–10, 2001.

[26] R. A. Johnson. alloy models with the embedded atom method. Physical Review B, 39(17):12554–12559, 1989.

[27] H. J. Lee, K. W. Kwon, C. Ryu, and R. Sinclair. thermal stability of a cu/ta multilayer: an intriguing interfacial reaction. Acta Materialia, 47(15-16):3965–3975, 1999.

[28] 2007. LAMMPS, Sandia National Laboratories: http://www.cs.sandia.gov/~sjplimp/.

[29] W. G. Hoover. canonical dynamics: equilibrium phase-space distributions. Physical Review A, 31(3):1695–1697, 1995.

[30] T. L. Hylton, B. Ciorneiu, D. A. Baldwin, O. Escorcia, J. Son, M. T. McClure, and G. Waters. thin film processing by biased target ion beam deposition. IEEE Transactions on Magnetics, 36(5):2966–2971, 2000.

[31] S. C. Seel, J. J. Hoyt, E. B. Webb III, and J. A. Zimmerman. modeling metallic island coalescence stress via adhesive contact between surfaces. Physical Review B, 73:245402.1–9, 2006.

[32] X. W. Zhou and H. N. G. Wadley. atomistic simulations of the vapor deposition of $ni/cu/ni$ multilayers: the effects of adatom incident energy. Journal of Applied Physics, 84(4):2301–2315, 1998.

[33] X. W. Zhou, H. N. G. Wadley, and S. Sainathan. low energy sputtering of nickel by normally incident xenon ions. Nuclear Instruments and Methods in Physics Research B, 234:441–457, 2005.

[34] W. D. Nix. mechanical-properties of thin-films. Metallurgical Transactions A - Physical Metallurgy and Materials Science, 20(11):2217–2245, 1989.

[35] X. W. Zhou and H. N. G. Wadley. misfit dislocations in gold/permalloy multilayers. Philosophical Magazine, 84(2):193–212, 2004.

[36] C. Günther, J. Vrijmoeth, R. Q. Hwang, and R. J. Behm. strained relaxation in hexagonally close-packed metal-metal interfaces. Physical Review Letters, 74(5):754–757, 1995.

[37] J. C. Hamilton and S. M. Foiles. misfit dislocation structure for close-packed metal-metal interfaces. Physical Review Letters, 75(5):882–885, 1995.

[38] X. W. Zhou and H. N. G. Wadley. the low energy ion assisted control of interfacial structure: ion incident energy effects. Journal of Applied Physics, 87(12):8487–8496, 2000.

[39] J. J. Quan, X. W. Zhou, and H. N. G. Wadley. low energy ion assisted atomic assembly of metallic superlattices. Surface Science, 600:2275–2287, 2006.

[40] J. J. Quan, X. W. Zhou, and H. N. G. Wadley. atomic assembly of metal surfaces and interfaces. Surface Science, 600:4537–4547, 2006.

[41] J. J. Quan, X. W. Zhou, and H. N. G. Wadley. low-energy ion-assisted control of interfacial structures in metallic multilayers. Journal of Crystal Growth, 300:431–439, 2007.

[42] Z. F. Li, W. S. Lai, and B. X. Liu. proposed interpretation for possible solid-state amorphization in some cu-based binary metal systems. Applied Physics Letters, 77(24):3920–3922, 2000.

[43] T. Egami. universal criterion for metallic glass formation. Materials Science and Engineering A, 226-228:261–267, 1997.

[44] C. Lin, G. W. Yang, and B. X. Liu. prediction of solid-state amorphization in binary metal systems. Physical Review B, 61(23):15649–15652, 2000.

[45] M. P. Anderson, D. J. Srolovitz, G. S. Grest, and P. S. Sahni. Computer simulation of grain growth - i. kinetics. Acta Metall., 32(5):783–791, 1984.

[46] I. Katzarov, S. Malinov, and V. Yanakieva. Mathematical modeling and numerical simulation of the formation and growth of a two-phase layer during diffusion in ternary system. Acta Meter., 53(10):3091–3099, 2005.

[47] J. W. Cahn. On spinodal decomposition. Acta Metall., 9(9):795–801, 1961.

[48] J. W. Cahn and J. E. Hilliard. Spinodal decomposition: A reprise. Acta Metall., 19:151–161, 1971.

[49] E. Bansch, P. Morin, and R. H. Nochetto. A finite element method for surface diffusion: the parametric case. J. Comp. Phys., 203(1):321–343, 2005.

[50] J. A. Sethian. Level Set Methods : Evolving Interfaces in Geometry, Fluid Mechanics, Computer Vision, and Materials Science. Cambridge University Press, Cambridge, 1996.

[51] H. Huang, G. H. Gilmer, and T. D. de la Rubia. An atomistic simulator for thin film deposition in three dimensions. J. Appl. Phys., 84(7):3636–3649, 1998.

[52] Y. G. Yang, R. A. Johnson, and H. N. G. Wadley. A monte carlo simulation of the physical vapor deposition of nickel. Acta mater., 45(4):1455–1468, 1997.

[53] C. L. Liu, J. M. Cohen, J. B. Adams, and A. F. Voter. Eam study of surface self-diffusion of single adatoms of fcc metals ni, cu, al, ag, au, pd and pt. Surf. Sci., 253(1-3):334–344, 1991.

[54] A. Swalin Richard. Thermodynamics of Solids. John Wiley & Sons, New York, 1972.

[55] M. H. Kalos and P. A. Whitlock. Monte Carlo Methods, volume 1. Wiley, New York, 1986.

[56] K. M. Chow, W. Y. Ng, and L. K. Yeung. Barrier properties of ni, pd and pd-fe for cu diffusion. Surf. and Coat. Technol., 105:56–64, 1998.

[57] M. Okada, J. Tao, and T. Nose. Dissolution of phase-separated domains after a jump to a temperature in the single-phase region. Polymer, 43(26):7429–7432, 2002.

[58] F. Reif. Fundamentals of Statistical and Thermal Physics. McGraw Hill, New York, 1965.

This page intentionally left blank.

DISTRIBUTION:

1 MS 9001
P.J. Hommert, 8000

1 MS 9001
P.A. Spence, 8000

1 MS 9004
J.M. Hruby, 8100

1 MS 9102
W.R. Even Jr., 8220

1 MS 9042
M.L. Chiesa, 8774

1 MS 9404
E.P. Chen, 8776

1 MS 9409
J.A. Zimmerman, 8776

5 MS 9402
X.W. Zhou, 8776

1 MS 9409
R.E. Jones, 8776

1 MS 9403
B.M. Wong, 8778

1 MS 9042
J.W. Foulk III, 8776

1 MS 9153
C.L. Knapp, 8200

1 MS 9161
A.E. Pontau, 8750

1 MS 9161
S.W. Allendorf, 8756

1 MS 9402
J.E.M Goldsmith, 8772

1 MS 9403
T.J. Shepodd, 8778

1 MS 9042
D.M. Kwon, 8770

1 MS 9405
R.W. Carling, 8700

1 MS 9409
C.D. Moen, 8757

1 MS 9402
R.A. Causey, 8758

1 MS 9161
N.C. Bartelt, 8756

1 MS 9161
J.C. Hamilton, 8756

1 MS 9161
K.F. McCarty, 8756

1 MS 9161
D.L. Medlin, 8756

1 MS 9401
A.L. Talin, 8756

1 MS 9161
K. Thuermer, 8756

1 MS 9403
A.M. Morales, 8778

1 MS 1315
N.A. Modine, 1132

1 MS 1411
E.B. Webb III, 1814

1 MS 1411
R.A. Roach, 1814

1 MS 1411
S.M. Foiles, 1814

1 MS 1322
J.B. Aidun, 1435

1 MS 1322
A.P. Thompson, 1435

1 MS 1322
P.A. Schultz, 1435

1 MS 1322
J. Robbins, 1435

1 MS 1322
P.S. Crozier, 1435

1 MS 0346
E.D. Reedy Jr., 1526

1 MS 9291
D. Robinson, 8755

1 MS 9161
D.F. Cowgill, 8758

1 MS 9409
G.J. Wagner, 8757

1 MS 9402
N.R. Moody, 8758

1 MS 1304
J.P. Sullivan, 1132

1 MS 1415
T.A. Friedmann, 1112

1 MS 0886
J.R. Michael, 1822

1 MS 9402
J.E. Smugeresky, 8758

1 MS 9402
B.P. Somerday, 8758

2 MS 9018
Central Technical Files, 8945-1

2 MS 0899
Technical Library, 4536

1 MS 0123
D. Chavez, LDRD Office, 1011